國立臺灣大學理學院大氣科學研究所

博士論文

Department of Atmospheric Science

College of Science

National Taiwan University

Doctoral Dissertation

熱帶季內振盪的辨識與對熱帶以外天氣的影響
—聚焦東亞冬季降水

Identification of MJO and its influences on extratropical weather focusing on East Asian winter rainfall

陳雲蘭

YUN-LAN CHEN

指導教授：隋中興 博士、張智北 博士

Advisors: Chung-Hsiung Sui, Ph.D., Chih-Pei Chang, Ph.D.

中華民國 112 年 8 月

August 2023

doi:10.6342/NTU202303152

中文摘要

本研究以奇異分解法（Singular Value Decomposition）發展一個 SVD2D_DJFM 熱帶季內振盪（MJO）冬季指標，來重新檢視 MJO 對熱帶以外區域天氣的影響。相較於廣為被應用的全季節性 RMM 指標（Wheeler and Hendon 2004），SVD2D_DJFM 更能解析出熱帶對流處於冬季氣候背景下，主要偶極冷、熱源在經向以及緯向的重要分布特徵；同時也更能掌握伴隨 MJO 熱帶波動、連結熱帶以外區域的大尺度環流結構。觀測資料分析顯示，SVD2D_DJFM 更能辨識出因為受到海洋大陸連結西太平洋附近（MCWP）冷源強迫力影響而導致的東亞降水。在東亞降水受 MJO 影響的波動周期中，MCWP 不論是單極型式或是以配搭印度洋反向熱源的偶極型式呈現，都是 MJO 熱帶冷、熱源強迫力的重要組成。MCWP 冷源對影響東亞天氣的重要性也透過線性斜壓模式（LBM）的數值模擬得到證實。與過去的研究所強調 MJO 印度洋熱源強迫力在南亞副熱帶引發向下游東傳的羅士培波列相比，MCWP 冷源造成的經向環流變化對東亞冬季降水的影響更為直接。此外，本研究指出菲律賓附近一個熱帶次中心（Sub_PH）的存在與否亦是 MCWP 冷源強迫力影響東亞降水的關鍵。Sub_PH 次中心伴隨整個 MCWP 冷源，於副熱帶區強化斜壓結構羅士培波環流的形成，為東亞帶來暖濕南來氣流，加上局地哈得里經向環流亦受 MCWP 對流抑制活動影響而減弱冬季風環流，都提供了東亞有利降水的環境條件。研究最後亦加入使用動力預報模式進行相關探究，發現 MCWP 冷源可影響模式對 MJO 波動的預報能力。在對流好發於印度洋的 MJO 事件中，具有 MCWP 冷源領先出現的分組類別能有更好的預報表現，研究結果顯示 MCWP 冷源對週尺度以上展期天氣預報的應用價值，也更加突顯 MCWP 冷源強迫力在 MJO 波動中的重要性。

關鍵詞：熱帶季內振盪、奇異分解法、冬季降水、羅士培波環流、局地哈得里經向環流

doi:10.6342/NTU202303152

Abstract

The influences of the Madden–Julian oscillation (MJO) on East Asian (EA) winter rainfall is revisited in this study by introducing an MJO index SVD2D_DJFM through a singular value decomposition (SVD) approach to resolve the seasonal-dependent spatiotemporal evolution of the MJO and associated circulation. This method uses two-dimensional instead of latitudinally averaged variables in the commonly used real-time multivariate MJO (RMM) index. A comparison of the two approaches is made and the result shows the SVD composite reveals a more conspicuous and coherent variation throughout the MJO cycle. In particular, the SVD analysis identifies the convection anomalies over Maritime Continent and Western Pacific (MCWP) as a major cause of enhanced rainfall in EA at RMM phases 8 and 1 (SVD phase S1–S2). Our research shows that the MCWP cooling is as important as the IO heating in the MJO phase (RMM P2–P3/SVD S3–S4) that was regarded the major cause of EA rainfall in most previous studies.

The observational analysis in our study suggests that the cooling and heating over MCWP, either in the form of monopole or dipole mode, is an important component of the MJO heating that results in stronger regional circulation along with subtropical Rossby wave responses influencing weather in East Asia. This suggestion is substantiated by linear baroclinic model (LBM) experiments that support the interpretation of the observational analysis, in that the MCWP-cooling induced anomalous meridional

doi:10.6342/NTU202303152

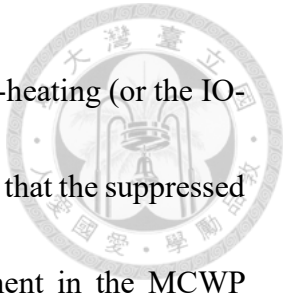

circulation is a more direct cause of enhanced EA rainfall than the IO-heating (or the IO-MCWP heating dipole) induced Rossby wave teleconnection. We note that the suppressed convection over east of Philippines (Sub_PH) is a critical component in the MCWP cooling that is coupled with significant baroclinic subtropical Rossby wave gyres, which bring low-level southerly warm flow to the EA region.

The important role of MCWP tropical forcing in the MJO cycle is further revealed in the prediction model. Our analysis shows MJO events carrying strong convection over Indian Ocean with a precursory MCWP cooling are more predictable in CFSv2 model than those without the precursory cooling. These results highlight the important role of the MWCP tropical forcing on the extended weather forecasts.

Keywords: Madden-Julian Oscillation; Singular Value Decomposition; Winter Rainfall; Rossby wave gyres; Meridional circulation

doi:10.6342/NTU202303152

Table of Contents

中文摘要 i

Abstract ii

Table of Contents iv

List of Tables vi

List of Figures vii

Chapter 1 Introduction 1

Chapter 2 The MJO index and data 5

2.1 Data 5

2.2 MJO structure 6

2.2a The leading modes of MJO convection 6

2.2b The large-scale circulation pattern associated with the MJO 8

2.2c The responses to tropical heating from numerical experiments 9

2.3 The requirement of the MJO index for a need on MJO regional impact study 13

2.4 A Singular Value Decomposition MJO index 14

2.5 Some statistical characteristics of the circulation based SVD index 17

Chapter 3 Evolution of EA winter rainfall through the MJO life cycle by SVD2D index 20

3.1 MJO-EA rainfall relationship based on RMM index 21

doi:10.6342/NTU202303152

3.2 Comparison of MJO-EA rainfall relationship based on SVD and RMM index 22

3.3 The sensitivity of the MJO-EA rainfall relationship to MJO indices 24

3.4 The MCWP- and IO-heating and their associated circulation related to EA rainfall 26

Chapter 4 The mechanism of MJO-EA rainfall relationship 30

4.1 Analysis of MJO-EA rainfall relationship based on SVD mode 2 30

4.2 Moisture budgets 32

4.3 Forced experiments by a Linear Baroclinic Model 34

Chapter 5 The effect of MCWP in the model prediction 39

5.1 Cases selection and the observational analysis 39

5.2 Comparison in model prediction 42

Chapter 6 Summary 46

Reference 49

doi:10.6342/NTU202303152

List of Tables

Table 1 Summary of the derivation of the MJO heating (Q_1') and the spatial distribution of (Q_1') imposed in the three experiments. 59

doi:10.6342/NTU202303152

List of Figures

Figure 1 Regressed daily OLR anomalies (OLR′) onto the PC of (a) EOF1 and (b) EOF2 of 25–90-day filtered OLR for extended winter (December to March). Daily OLR′ is obtained by removing seasonal cycle and the previous 120-day mean. 60

Figure 2 Regressed OLR, streamfunction (contours, unit: $10^{-6}m^2s^{-1}$) and vector wind at (a) 200-hPa and (b) 850-hPa, against the EOF1 of 25–90-day filtered OLR for extended winter (December to March). 61

Figure 3 Same as Fig. 2, except for EOF2. 62

Figure 4 The simulated 200-hPa stream function at day 5 in response to four idealized heating (heating and cooling shaded in red and blue) in He et al. (2011): (a) H120 (b) H90C165. 63

Figure 5 Same as Fig. 1, except for SVD_U index. 64

Figure 6 Same as Fig. 1, except for SVD_O index. 65

Figure 7 Regressed OLR, streamfunction (contours, unit: $10^{-6}m^2s^{-1}$) and vector wind at 200-hPa against EOF1 of (a) SVD_U, and (b) SVD_O index for extended winter (December to March). 66

Figure 8 Same as Fig. 7, except for EOF2. 67

Figure 9 The power spectra of the reference time series of the (a) SVD_U mode 1, (b)

doi:10.6342/NTU202303152

SVD_U mode 2, and (c) their coherence square, derived from the SVD2D_DJFM analysis. 68

Figure 10 The average number of MJO days in each of the 12 calendar months, 1980–2015. The MJO days are defined by the amplitude of the MJO index, SVD2D_DJFM (red bars) and all-season RMM (blue bars), larger than > 1. 69

Figure 11 Composites of anomalous GPCP rainfall and winds at 200-hPa (black arrow) for 8 MJO phases based on (a) SVD2D_DJFM index and (b) RMM index. 70

Figure 12 MJO phase diagram based on (a) SVD_U index and (b) all-season RMM index for a winter season from December 2015 to March 2016 when two successive MJOs occurred. 71

Figure 13 Climatological mean of (a) Height (contour), (u, v), and wind speed (light shadings) at 200-hPa; (b) (u, v) at 850-hPa and GPCP precipitation for extended winter season (DJFM) based on 1980–2015. 72

Figure 14 Climatological mean meridional-vertical cross section of (v, w), potential temperature (colored), and relative humidity (contoured in green) within 120°-130°E for extended winter season (DJFM) based on 1980–2015. 73

Figure 15 Probability distribution of rainfall anomalies within the EA region in the 8 phases of the MJO defined by all-season RMM index. 74

doi:10.6342/NTU202303152

Figure 16 Composites of anomalous GPCP rainfall and winds at 850-hPa in RMM Phase 2 for (a) top 1/3 and (b) bottom 1/3 of days sorted out by the frequency distribution of GPCP rainfall anomalies averaged in East Asian region marked by the black rectangle. 75

Figure 17 Composites of anomalous GPCP rainfall and winds at 850-hPa (gray arrow) and 200-hPa (black arrow) in RMM Phase 8-1-2-3 for top 1/3(Left) and bottom 1/3(Right) of days arranged by the frequency distribution of averaged GPCP rainfall anomalies in East Asian rainfall region. 76

Figure 18 Composite fields of anomalous GPCP rainfall and 850-hPa wind for the half cycle of the MJO (P8, P1, P2, P3) defined by all-season RMM and (S1, S2, S3, S4) by SVD2D_DJFM. The composite fields are shown in the order of four phases (a, b) P8, S1, (c, d) P1, S2, (e, f) P2, S3, (g, h) P3, S4. The unit of GPCP and wind is mm day^{-1} and m s^{-1}. 77

Figure 19 Probability distribution of rainfall anomalies within the EA region in the 8 phases of MJO defined by SVD index. 78

Figure 20 Rainfall anomalies in the EA region (110°E~150°E; 20°N~35°N) displayed in the (PC1, PC2) phase space based on (a) RMM, and (b) SVD indices. 79

Figure 21 Probability distribution of rainfall anomalies within the EA region in the 8 phases of MJO defined by different approaches: (a) SVD_U index (b) SVD_O

doi:10.6342/NTU202303152

index (c) SVD_U index based on data within 15°S–15°N (d) BPOLR_25–90d index (e) All-season RMM index (f) RMM DJFM index. 80

Figure 22 MJO phase composite fields of anomalous GPCP rainfall and winds at 850-hPa for phase S2–S4 (WH04 RMM phase P1–P3, from top to bottom): (a) SVD_U, (b) SVD_U index based on data within 15°S–15°N, (c) 25–90-day filtered OLR, (d) RMM_DJFM. 81

Figure 23 Anomalous fields of GPCP rainfall (shaded), 200-hPa height (contour) and 200-hPa wind (arrow) composite for SVD phase (a) S1, (c) S2, (e) S3, (g) S4, (i) S5, for days the EA rainfall larger than the threshold at top 1/3 of frequency distribution of daily GPCP rainfall averaged in East Asia (20°N–35°N,110°E–150°E). (b, d, f, h, j) the same as (a, c, e, g, i) except for 850-hPa temperatures (shaded), 500-hPa height (contour) and 850-hPa wind (black arrow). 82

Figure 24 Same as Fig. 23, except for SVD phase S5, S6, S7, S8, S1 for days the EA rainfall smaller than the threshold at bottom 1/3 of frequency distribution of daily GPCP rainfall averaged in East Asia (20°N–35°N,110°E–150°E)..... 83

Figure 25 Composite fields of anomalous GPCP rainfall and 200-hPa winds for the days when PC2 of the SVD analysis < 1σ and (a) PC1 < 0, (b) PC1 > 0..... 84

Figure 26 Same as Fig. 25, except for anomalous temperature at 850-hPa (colored)

doi:10.6342/NTU202303152

and heights at 500-hPa (contoured) and 850-hPa winds (vector). 85

Figure 27 The horizontal fields of vertically integrated moisture budget: (a),(b) horizontal advection for SVD12 and SVD34 and (c),(d) vertical advection for SVD12 and SVD34 (units are g kg^{-1}day^{-1}). The positive values are shaded and also contoured. 86

Figure 28 As in Fig. 27, but for the dominant component $-(<\widetilde{\boldsymbol{v}'}\cdot\nabla\bar{q}>)$ and $-(<\widetilde{\omega'}\partial_p\bar{q}>)$(g kg^{-1}day^{-1}). The positive values are shaded and also contoured. 87

Figure 29 The areal mean of vertically integrated moisture budget within the EA region (110ºE–150ºE, 20ºN–35ºN) for SVD phase 1–2 and SVD phase 3–4. The budget terms shown include the tendency, Hadv, Vadv, and *R* = $-L^{-1}\left(<\widetilde{Q_2}>-\overline{Q_2}\right)$ (units are g kg^{-1}day^{-1}). 88

Figure 30 (a)–(c) The horizontal distribution of vertically integrated $Q1'$ and (d)–(f) the vertical–zonal distribution of latitudinally averaged $Q1'$ within 15ºS–15ºN for SVD12, MCWP, and SVD34, respectively. Units are K day^{-1}. Thin solid and dashed lines enclosing the heating and cooling fields in (a)–(c) are 0.2 and –0.2 K day^{-1} contours. 89

Figure 31. Model simulated fields in SVD12 (a) horizontal wind (vectors), height (contour; interval 10 m), and velocity potential (shading) at 230 hPa, (b) vertical velocity at 550 hPa (shading) along with $Q1' =$ 0.2 and –0.2 K day^{-1}

doi:10.6342/NTU202303152

contours (as in Fig. 30a), and (c) horizontal wind (vectors), height (contour; interval 2 m) at 900 hPa. 90

Figure 32 As in Fig. 31, but for MCWP. 91

Figure 33 As in Fig. 31, but for SVD34. 92

Figure 34 The MJO phase diagram for (a) 19 ISO-A and (b) 12 ISO-B events..... 93

Figure 35 Composite evolution of averaged tropical (15°S-15°N) rainfall anomalies for (a) ISO-A and (b) ISO-B events. 94

Figure 36 Composite evolution of rainfall, 200-hPa height, and 850-hPa winds at day -10, -5, 0, +5 for (a) ISO-A and (b) ISO-B events..... 95

Figure 37 Composite time-longitude section of rainfall, 200-hPa height, and 850-hPa winds averaged within 110°E-120°E for (a) ISO-A and (b) ISO-B events..... 96

Figure 38 Composite evolution of averaged tropical (15°S–15°N) rainfall and 850-hPa zonal wind anomalies in time (day -20 to day 20) and longitude (80°E-180) for (a) observations and NCEP CFSv2 forecasts at lead time (b) 8 days (c) 16 days, (d) 24 days (e) 32 days for ISO-A events. (f)-(j) same as (a)-(e) except for ISO-B events. 97

Figure 39 The pattern correlation between the observation and NCEP CFSv2 forecast of rainfall evolution in time (day -20 to day 20) and longitude (80°E-180) as in Fig. 38. The forecast lead time ranges from day 0 to day 45. The pattern

doi:10.6342/NTU202303152

correlations for ISO-A and ISO-B are shown in blue and red, respectively... 98

Figure 40 The time-latitude section over 15°N–30°N of rainfall anomalies (colored) and 200-hPa height anomalies (contour) and 850-hPa winds (vector) averaged over 110°E–120°E for (a) observations and NCEP CFSv2 forecasts at lead time (b) 8 days (c) 16 days, (d) 24 days (e) 32 days for ISO-A events. (f)-(j) same as (a)-(e) except for ISO-B events..... 99

doi:10.6342/NTU202303152

Chapter 1 Introduction

The tropical 40-50-day oscillation in surface pressure, wind, and precipitation first discovered by Madden and Julian (Madden and Julian 1971, 1972) is a dominant eastward-moving planetary scale quasi-periodic disturbance. This intra-seasonal-scale disturbance has received numerous studies and is now commonly referred to as Madden-Julian Oscillation (MJO) (e.g., Zhang 2005; Jiang et al. 2020). These studies reveal that the MJO associated convective heating, although confined in the tropics, can force Rossby wave trains that propagate out of tropics in 1-2-week time scale (e.g., Ferranti et al. 1990; Jin & Hoskins 1995; Zhang 2013).

The persistent MJO and associated Rossby wave trains modulate extreme weather and climate events in various tropical and extratropical regions such that the MJO has been identified as an important source of sub-seasonal predictability and a critical component in the seamless forecasts to bridge the weather and climate (e.g., Zhang 2013). The global influences of the MJO and its potential predictability up to several weeks make it a priority target of research-to- operation development in major weather agencies. An improved forecast system in sub-seasonal prediction can add great values to disaster-prevention decisions by policy makers.

Understanding and prediction of the MJO has drawn many studies as revealed in

doi:10.6342/NTU202303152

comprehensive reviews in Madden and Julian (1994), Zhang (2005, 2013), Jiang et al. (2020), Li et al. (2020), and Lin (2022). These studies have established a broad knowledge base that benefits the forecast applications in the worldwide operational centers (e.g., Gottschalck et al. 2010; Waliser and Sperber 2015; Wheeler et al. 2017). Continuous efforts on the MJO researches would maximize its value of sub-seasonal predictability.

The MJO is connected to many weather–climate systems, its structure and its interaction with other weather–climate phenomena are crucial to its global influence. Even though many studies on MJO impact have revealed its relationship with weather in different climate regions, to test the statistical significance of MJO effects on global weather–climate phenomena rigorously is greatly needed (e.g., Ling et al. 2017). The focus of this study is the influence of MJO on the extra-tropical weather, particularly on East Asia region in the winter season.

Tropical-extratropical interactions play an important role for the MJO and its global influence (e.g., Stan et al. 2017). Many studies have demonstrated the MJO influence on the extra-tropical is associated with atmospheric response to tropical heating and its interaction with extratropical variability, such as the Pacific North America (PNA) and North Atlantic Oscillations (NAO) (e.g., Hoskins and Karoly 1981; Ferranti et al. 1990; Matthews et al. 2004; Cassou 2008; Lin et al. 2009). The MJO heating and its divergence outflow in the upper troposphere excite the extratropical Rossby wave responses which

doi:10.6342/NTU202303152

further interact with the westerly mean flow in the region. Under favorable conditions, the extratropical Rossby wave excited from the tropical heating can develop further by extracting energy from the background mean flow. Therefore, the climatological jet position and its variabilities play a key role in the MJO's influence. Previous studies also have found extratropical Rossby wave responses are sensitive to the longitudinal location of the tropical forcing (e.g., Simmons et al. 1983; Ferranti et al. 1990; Matthews et al. 2004; Kim et al. 2006; He et al. 2011; Seo and Son 2012; Zheng and Chang 2019). A dipole heating over Indian Ocean and western Pacific was shown to correspond to more significant extratropical wave activities than a monopole forcing does (e.g., Matthews et al. 2004; Lin et al. 2010; He et al. 2011). Tseng et al. (2019) found the dipole heating in specific MJO phases (phase 2, 3, 6, 7) favors a more consistent teleconnection pattern. In addition to the tropic intra-seasonal variabilities (ISV), extra-tropics have its own source of ISV, and the two can interact with each other through complex mechanisms. Hsu (1996) proposed a global view of the ISV involving equatorial wave dynamics, tropical-extratropical interactions and eddy-mean flow interactions.

The connection between the MJO phases and regional variabilities of precipitation and surface air temperature have also been investigated in many different climate regions. One of the areas with most significant correlation with the MJO cycle is North America because of its downstream location in the aforementioned MJO-PNA teleconnection. Mo

doi:10.6342/NTU202303152

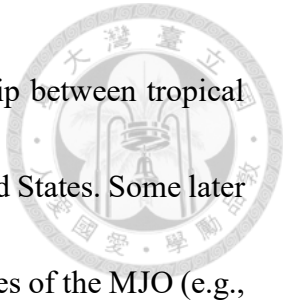

and Higgins (1998) is one of the earlier studies about the relationship between tropical convection of the MJO and precipitation regimes in the western United States. Some later studies documented the weather over North America in different phases of the MJO (e.g., Lin et al. 2010; Becker et al. 2011; Jones and Carvalho 2012; Zheng et al. 2018). These studies revealed a 2–3-week lag of North American signals to the peak of MJO activities over IO and WP and attribute the time scale a result of Rossby wave propagation. Concerning the MJO impact on East Asia, the Rossby wave responses to the MJO heating over Indian Ocean and western Pacific were also applied as a mechanism (e.g., Kim et al. 2006; Jeong et al. 2008; Jia et al. 2011; Hung et al. 2014; Yao et al. 2015; Song and Wu 2019). In addition, He et al. (2011) proposed a direct MJO influence.

In this thesis, we zoom in the importance of identifying the MJO events for studying the MJO's influence on extratropical region. More specifically, we focus on the identification of the MJO by a set of indices. We propose an MJO index defined by the Singular Value Decomposition (SVD) analysis (e.g., Bretherton and Wallace 1992) to address some critical concerns. The SVD index is introduced in Chapter 2. The MJO influences on EA are examined in Chapter 3. The fundamental role of MCWP heating anomalies is presented in Chapter 4. The benefit of SVD-identified heating patterns in MJO prediction is discussed in Chapter 5. A summary is given in Chapter 6.

doi:10.6342/NTU202303152

Chapter 2 The MJO index and data

A concise and quantitative description of the MJO evolution (structure, propagation, intensity, lifetime) is fundamentally important for studying the MJO and its global influence. This has motivated us to design a new MJO index and to perform a comparative review of commonly used MJO indices for identifying the MJO evolution. In this chapter, the data used for the current study is introduced in 2.1. We first adopt a commonly used index for describing the MJO structure in Chapter 2.2. We then discuss the requirements for defining the MJO index in Chapter 2.3. In Chapter 2.4, we introduce an MJO index based on the SVD approach that is one of the major efforts of this study. The salient features of the MJO characteristics based on the SVD index is discussed in Chapter 2.5.

2.1 Data

The rainfall data used for this study are the Global Precipitation Climatology Project (GPCP) merged analysis of pentad precipitation (e.g., Xie et al. 2003) on a global 2.5° latitude X 2.5° longitude grid for the period 1979–2016. The pentad precipitation data are converted to daily data by first applying the pentad rainfall to each of the five days, and then using a 5-day running mean through the entire time series of each season. The EA rainfall is defined as the area mean of the rainfall over 110°–150°E, 20°–35°N. The outgoing longwave radiation (OLR), which is closely related to rainfall in the tropics, is

doi:10.6342/NTU202303152

used to represent tropical convective activity. We use the new climate data record for daily OLR (e.g., Lee and NOAA CDR Program 2011; Schreck et al. 2018) from the High-Resolution Infrared Radiation Sounder (HIRS) sensors. The data are regridded to a global 2.5° X 2.5° resolution from its original 1.0° X 1.0° resolution. The daily wind variables used in this study are derived from National Centers for Environmental Prediction–Department of Energy (NCEP–DOE) atmospheric reanalysis (e.g., Kanamitsu et al. 2002). They are also on 2.5° X 2.5° grids.

2.2 MJO structure

As a reference for discussing the SVD based index for MJO, we first discuss the robust MJO structure in this sub-section. The MJO structure is shown in three aspects: the leading modes of the MJO (2.1a), the large-scale circulation patterns associated with the MJO (2.1b), and the responses of tropical heating from numerical experiments (2.1c).

2.2a The leading modes of MJO convection

The MJO is commonly represented by the dominant spatial pattern and corresponding time evolution in tropical convection by empirical orthogonal function (EOF) analysis of band-pass filtered data. The two leading EOF modes were often used for representing the main tropical heating patterns of the MJO and for composing an index to describe the propagation of the MJO. For demonstrating the leading pattern of the MJO

doi:10.6342/NTU202303152

convection, an EOF analysis of 25–90-day filtered OLR for extended winter (December to March, DJFM) was performed. The 2 leading modes shown in Fig. 1 account for 10% and 9% of the total variance. Both EOF modes show that MJO convection oscillates in zonal dipole form within tropical Indo-Pacific warm pool. The EOF1 is characterized by a negative pole over eastern Indian Ocean and Maritime Continent (IOMC, roughly 90°E–140°E), and the positive pole over central Pacific (CP, roughly 170°E–150°W). EOF2 also exhibits a dipole structure with positive anomalies over Indian Ocean (IO, roughly 60°E–100°E), and negative anomalies over Maritime Continent and Western Pacific (MCWP, roughly 120°E–170°E). In this study, we name the EOF1 dipole pattern as IOMC-CP mode, and EOF2 dipole pattern as IO-MCWP mode.

In additional to the zonal dipole structure, the two EOFs also show meridionally-oriented double peaks in the Indo-Pacific warm pool. The peaks south of the equator have larger anomalies especially at the climatological position of SPCZ (Sub_SPCZ). The other subcenter resides east of Philippines over Western Pacific (Sub_PH). It's interesting to point out an area of significant anomalies over subtropical north Pacific (Sub_CP) next to Sub_SPCZ and Sub_PH. The Sub_CP appears to form a dipole with Sub_PH in the N.H. subtropical region. Notice that anomalies over EA only appear significantly in the IO-MCWP mode, but not clear in the IOMC-CP mode.

The MJO convection features in Fig. 1 differ in details from other studies due to

doi:10.6342/NTU202303152

differences in the observational data, space and time filtering, and analysis approaches. Extra-tropical response is very sensitive to the longitudinal position of the tropical heating as will be shown next.

2.2b The large-scale circulation pattern associated with the MJO

Observational analysis and theory studies have shown the MJO is a slowly eastward-propagating super cloud cluster coupled with planetary-scale circulation. The composite MJO resembles the forced Kelvin-Rossby solution to a stationary tropical heating (e.g., Gill 1980). But the MJO properties might differ along its eastward-propagating path with the change of the background mean state (e.g., Zheng and Chang 2020). To show the circulation pattern associated with the MJO, regression maps based on the index constructed by the two leading EOFs of OLR mentioned in last section are used here. More comprehensive description of the 3-dimensional structure of the MJO can be seen in Kiladis et al. (2005), Adames and Wallace (2014).

The regression map of large-scale circulation pattern associated with EOF1 and EOF2 of 25–90-day filtered OLR for extended winter are shown in Fig. 2 and Fig. 3. Corresponding to the EOF1 dipole heating (IOMC-CP), the circulation shows a pair of anti-cyclonic gyres at 200-hPa (Fig. 2a) and cyclonic gyres at 850-hPa (Fig. 2b) to the left of the convection region at IOMC. Another pair of cyclonic gyres at 200-hPa and anti-

doi:10.6342/NTU202303152

cyclonic gyre at 850-hPa appear over CP where the equatorial cooling is located. Notice that the cyclonic Rossby wave gyre in northern latitudes at 850-hPa is roughly within 30°N, while the anti-cyclonic Rossby wave gyre at 200-hPa skews to the north and extends further into 40°N. An MJO index based on symmetric concept might not be able to describe this kind pattern completely.

For the EOF2 (Fig. 3), which with the IO-MCWP dipole pattern, the pair of anti-cyclonic(cyclonic) Rossby wave gyres symmetric to near the equator flanks to the left of the MCWP convection region in 200-hPa (850-hPa). To the left of the IO convection region, the strength of the Rossby wave gyres is far weaker than its counterpart in this dipole pair. It seems that the MCWP forcing is more critical than IO forcing for EA midlatitude response. This MCWP flanking Rossby wave gyres center near 120°E with a strong anti-cyclone(cyclone) occupy the region of south China Sea to east of Philippines, where shows clear meridional overturning circulation inducing from the MCWP heating. The MCWP heating seems an important direct influence of the MJO forcing.

In general, the above circulation features in northern hemisphere is generally considered tropical-extratropical interactions. In this study, we look into the problem by focusing on the influence of the MJO on the East Asia. Some relevant modeling studies are reviewed in the next sub-section.

2.2c The responses to tropical heating from numerical experiments

doi:10.6342/NTU202303152

Many observational and modeling studies have shown waves develop in response to the MJO convective heating and propagate out of the tropics while growing to form wave trains (e.g., Hoskins and Karoly 1981; Simmons et al. 1983; Jin and Hoskins 1995; Matthews et al. 2004; Seo and Son 2012). Modeling studies further suggest that the wave trains are maintained either by energy conversion from the midlatitude mean flow through barotropic or baroclinic instabilities. So, the background state of the jet stream plays an important role in extratropical responses to the MJO. In addition, baroclinic instabilities maintain organized storm tracks that further alter the mean state. Since the response to the MJO heating in any particular phase evolves in a time scale of 2 weeks, the response to a propagating MJO event will, in general, be the sum of responses to the tropical heating at different locations and times. As a result, we must consider background state of the Jet stream as well as spatial distribution of the MJO heating in understanding the responses of extratropical responses to the MJO. In this subsection, we will review some previous modeling studies on the MJO influences on wintertime weather especially in East Asian region. For a more comprehensive review of many existing studies about tropical-extratropical teleconnections on intra-seasonal time scales, we refer to a recent review article by Stan et al. (2017).

Simmons et al. (1983) performed one of earlier numerical study on the MJO teleconnection. They tested a set of 10-day integrations with the location of forcing

doi:10.6342/NTU202303152

maximum varied in latitude from 10°S to 30°N at an interval of 5° latitude and 15° longitude in the global tropics. They showed the regions of preferred responses are over the northeastern Pacific and Atlantic. They also found responses over the northeastern Pacific are most easily excited by forcing located over Southeast Asia and the tropical northwest Pacific Ocean. On studying tropical-extratropical interaction associated with the 30–60-day oscillation, Ferranti et al. (1990) used a barotropic model forced by the observed EOFs of OLR to test and confirm the existence of the mode of barotropic instability exciting by MJO tropical forcing. In their analysis, they also inferred the presence of a convective center east of the Philippines excites the PNA positive phase. Matthews et al. (2004) use a primitive equation model initialed with climatological mean flow and forced with a time-dependent heating derived from the observed MJO heating anomalies to examine the cause of the MJO circulation anomalies. They confirmed that the MJO has an associated global evolving circulation that is predominantly a direct response to its tropical heating anomalies, where the tropical convective outflow anomalies lead to Rossby wave sources. They also point out the eastward propagation of the excited Rossby wave are guided by the ambient jet and are able to extract emerge from it in a manner similar to that of unstable barotropic normal modes.

Lin et al. (2010) used a linearized global primitive equation model to examine the impact of the MJO on winter precipitation in Canada. Based on the two leading EOF

doi:10.6342/NTU202303152

modes of the MJO convection, they found the 1–3 pentad lagged responses to a specific dipole thermal forcing in the Indian Ocean and western Pacific (similar to the MJO convection in RMM phase 2–3) resembles the observed circulation anomalies. They also designed experiments to test heating at different longitude, they found maximum contributions come from a heating source near 80°E and a cooling source near 160°E, and explained why a dipole convection pattern of their EOF2 is so effective in forcing an extratropical circulation anomaly, because of the superposition of the responses to the dipole heating.

On the studies focusing on East Asia, He et al. (2011) proposes the MJO impacts on the EA winter weather through changing the local Hadley cell and the northward extension of the equatorial Rossby wave response. To test the hypothesis, they conducted two linear experiments with idealized tropical heating (Fig. 4): heating at 120°E (H120); and heating at 90°E and cooling at 165°E (H90C165). The idealized monopole and dipole heating in H120 and H90C165 are based on their EOF1 and EOF2 that are similar to the EOF analysis of OLR in Fig. 1. Their model responses to the H120 (Fig. 4a) and H90C165 (Fig. 4b) show a similar quadrupole flow but the latter is shifted westward and of much stronger magnitude relative to the former. They also noted stronger westerlies wind in H120 over northern China and Japan and related it to variation of the East Asian jet and local Hadley circulation in addition to the Rossby wave responses to the heating.

doi:10.6342/NTU202303152

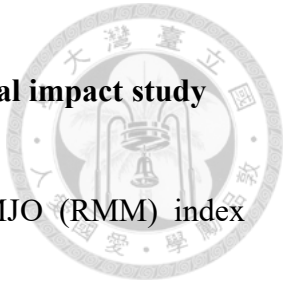

2.3 The requirement of the MJO index for a need on MJO regional impact study

Among published MJO indices, the real-time multivariate MJO (RMM) index developed by Wheeler and Hendon (2004, WH04) is widely used in the MJO research and prediction. The RMM index gains its popularity for several reasons. Frist, the use of OLR and zonal wind at 850-hPa and 200-hPa averaged within equatorial band 15ºN–15ºS and the combined EOF (CEOF) analysis of the variables is a simple yet sufficient approach to extract the first-baroclinic, equatorial-symmetric, convection-coupled circulation (e.g., Wang and Rui 1990). Second, data processing procedure of rolling forward averages make it easier for the real-time applications. Third, the index is defined for all seasons.

While RMM index is widely used, possible problems or limitations have been discussed. Roundy et al. (2009) pointed out that the EOF based index is derived by summation of data projection from locations and variables such that the index can be contributed by non-MJO associated signals. Straub (2013) demonstrated that RMM is dominated by its circulation components, so it is more representative of the large-scale zonal circulation, but not an appropriate measure of convective MJO initiation. They suggested that the choice of MJO index depends on whether the focus is on convection or circulation. Ventrice et al. (2013) proposed to use 200-hPa velocity potential to replace OLR component in the RMM, so that they can enhance the divergence signal in the

doi:10.6342/NTU202303152

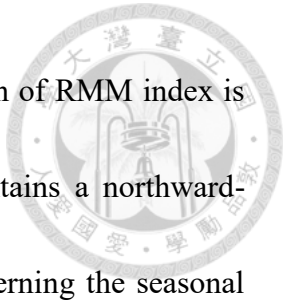

Pacific sector for their interests on tropical cycles. Another limitation of RMM index is on tracking the boreal summer intra-seasonal oscillations that contains a northward-propagating component besides the eastward-moving signals. Concerning the seasonal dependent issue, Kikuchi et al. (2012) proposed a bimodal ISO index by considering EOF mode in winter (DJF) and summer (JJA). The winter EOF mode features dominant eastward-propagating signals along the equator that is often called the MJO while the summer EOF mode contains additional northward-propagating signals that is referred to as Boreal Summer ISO (BSISO). A regional BSISO was proposed by Lee et al. (2013) for Asian summer monsoon region that is adopted in the APEC Climate Center operational products. The above studies indicate that the choice of index depends on specific applications.

The MJO impact on extra-tropical East Asia winter rainfall variation is the main interests in this study, our analysis (will present in the Chapter 3) shows the RMM index performs well in describing the overall MJO eastward-propagating in all season, yet it is not designed to highlight season-dependent features that are strong in East Asia region like the meridional distribution of the MJO heating and the associated teleconnection waves. For this consideration, 2-dimension fields covering the zonal and meridional structure of the MJO in winter are required.

2.4 A Singular Value Decomposition MJO index

doi:10.6342/NTU202303152

We develop a winter-season MJO index using 2-dimensional fields, instead of the meridionally averaged 1-dimensional series as in all-season RMM index (WH04), through an SVD approach. The SVD method extracting the maximum covariance from a pair of data matrix, which can be used to extracting the convection-circulation coupled pattern by designing the pair of data consisting of OLR (arranged in the left vector in SVD analysis) and two zonal wind fields (arranged in the right vector in SVD analysis). The OLR serves as a proxy for tropical heating, the data domain covers the same global tropical belt (15ºS–15ºN) as in the RMM index. For zonal wind fields at 850 and 200 hPa, the domain is expanded northward to cover the area of 15ºS–30ºN so that a substantial part of subtropical Rossby wave gyre associated with the MJO is included. By seeking singular vectors of maximum covariance, the SVD solves for the most dominant convection-circulation coupled pattern. As such, the SVD method is more suited for extracting the MJO heating and associated circulation than the combined EOF method used for deriving RMM index. Indeed, previous studies demonstrated that the RMM index tends to be influenced more by zonal wind than OLR (e.g., Straub 2013).

The data filtering procedures is the same as in WH04. The main procedures are as follows : 1) Removal of the seasonal cycle by subtracting the mean and the first three harmonics of the annual cycle; 2) Removal of the inter annual variability by subtracting the previous 120-day mean from each day for each grid point; A removal of the El

doi:10.6342/NTU202303152

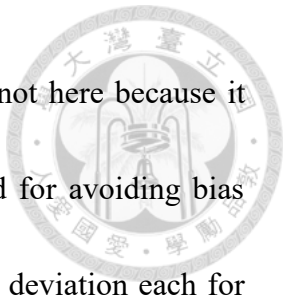

Niño/Southern Oscillation (ENSO) signal is applied in WH04, but not here because it makes not much difference; 3) A normalization process is designed for avoiding bias toward specific variable by dividing by the mean temporal standard deviation each for U850 and U200, the two fields which are combined in the SVD right vector.

The SVD approach produces two sets of MJO index: one is OLR-based SVD index (SVD_O) by projecting the OLR data on the two leading pairs of singular vectors of OLR component. The other is circulation-based SVD index (SVD_U) by projecting the U850 and U200 data on the two leading pairs of singular vectors of circulation component. The anomalous OLR regressed against the leading pair of SVD_U and the leading pair of SVD_O are shown in Fig. 5 and Fig. 6, respectively. The regressed OLR patterns on the two SVD index resemble each other with the IO-MCWP pattern as a robust feature.

To check if OLR-base SVD index is necessarily better for the MJO impact study, we show the regression maps on circulations at 200-hPa based on SVD_U and SVD_O associated with the first and second SVD mode in Fig. 7 and Fig. 8, respectively. The high similarity between the patterns from SVD_U and SVD_O show circulation-based SVD index perform as well as OLR-based SVD index. We chose SVD_U in this study as the index to study the MJO impact on EA weather because the Rossby wave gyre in the subtropical play an important role for the MJO impact on extratropic. Hereafter, the index is referred to as SVD2D_DJFM. Some characteristics of SVD2D_DJFM are discussed in

doi:10.6342/NTU202303152

the next subsection.

2.5 Some statistical characteristics of the circulation based SVD index

To show the variability of SVD2D_DJFM and the associated MJO characteristics, we first apply a power spectrum analysis to the time series of the first two leading SVD modes. Although the projected time series is unfiltered, the analysis (Fig. 9) shows significant spectral peaks in the frequency band between 30–80 days for both mode 1 and mode 2 and the variability of the two modes in the spectral band are highly coherent.

We then count statistics of significant MJO days by checking the daily amplitude of the MJO index that is larger than one standard deviation. The number of significant MJO days in each of the 12 calendar months for both SVD2D_DJFM and all-season RMM is shown in Fig. 10. The figure shows that the all-season RMM index identifies about 16–18 significant MJO days in both warm and cold seasons while the SVD2D_DJFM identifies similar number of days only in cold season (DJFM). The contrast between the two index arises obviously from the use of data that consider winter season only and all four seasons that resolves respectively the winter only and common year-round features of the MJO. The contrast is also attributable to the derivation of RMM from equatorial symmetric OLR and zonal winds by averaging the variables in 15°S–15°N latitudinal band.

doi:10.6342/NTU202303152

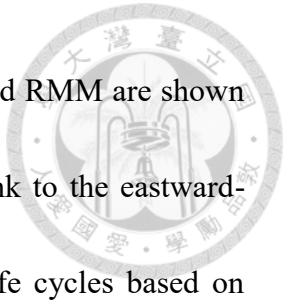

Composite maps for an MJO cycle based on SVD2D_DJFM and RMM are shown in Fig. 11. The coupled Rossby wave circulation is seen closely link to the eastward-propagating tropical convection. Comparing the composite MJO life cycles based on SVD2D_DJFM (Fig. 11a) and all-season RMM (Fig. 11b), the overall evolution in the two figures are quite similar except differ by 1/8 phase difference, i.e. RMM phase 2–3 corresponds to SVD phase 3–4, and RMM phase 8–1 corresponds to SVD phase 1–2. But the SVD-based composite shows more significant signals in extratropical wave trains corresponding to the MJO heating.

The phase shift is further revealed in the MJO phase diagram based on all-season RMM index and SVD2D_DJFM index (Fig. 12) of the successive MJO occurred in December 2015–March 2016. The sequences for the MJO event in the phase diagram trace two and half circles from early December to end of March that corresponds to an average 50-day life time for a circle. The circling tracks of the two indices show similarly in the eastward propagation, but the evolution of the MJO in the RMM phases differ from the SVD phases by 1/8 of a cycle. The difference in magnitude reflect the difference in leading modes of the two MJO indices

The MJO phase diagram follows WH04 who plotted pairs of daily PC1 and PC2 of the combined EOF analysis of OLR and zonal wind (i.e. all-season RMM index) in x- and y- cartesian coordinate. Since the tropical convection pattern of the 2 leading modes

doi:10.6342/NTU202303152

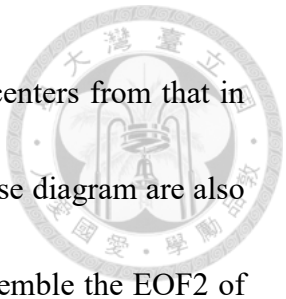

of SVD2D_DJFM differ in longitudinal locations of major heating centers from that in all-season RMM index, their projections on daily OLR shown in phase diagram are also different. For example, the RMM phase 2–3/6–7 (P2–P3/P6–P7) resemble the EOF2 of WH04 that features an IO dominatant heating, while the SVD2D_DJFM phase 2–3/6–7 (S2–S3/S6–S7) resemble the mode 2 of SVD in this study that shows an IO-MCWP dipole heating. Also note that MCWP heating is more dominant in S2/S6, while IO heating is more dominant in S3/S7. An interesting observation from the MJO event in Fig. 12 is that the MJO heating represented by SVD2D_DJFM index highlight the MCWP heating in S1-S2 (Fig. 12a) that is least evident in the RMM phase diagram (Fig. 12b). Next in Chapter 3, we investigate the MJO modulation of EA winter rainfall by SVD2D_DJFM index.

doi:10.6342/NTU202303152

Chapter 3 Evolution of EA winter rainfall through the MJO life cycle by SVD2D index

Weather in the East Asia (EA) region is strongly influenced by baroclinic waves in EA winter monsoon (EAWM) as shown in Fig. 13. The EAWN consists of East Asian (EA) trough and westerly jet stream along 30°N from Eastern China to near the dateline at 200-hPa (Fig. 13a) and Siberia Mongolia High (SMH) over Eurasia and the Aleutian Low over the northern Pacific (Fig. 13b). The mean precipitation in Fig. 13b shows significant rainfall in the tropical warm pool region within 20°S–10°N. Also notable is the rain band north of 20°N from southern China to North Pacific that is the storm track of midlatitude cyclones and the usual destination of frontal systems. The East Asian winter monsoon also features strong tropical-extratopical coupled circulation as shown by the mean vertical and meridional cross section of meridional and vertical winds, potential temperature (θ) and relative humidity within 120°E–130°E (Fig. 14).

The area of 20°N–35°N and 110°E–150°E (the rectangle in Fig. 13) is defined for calculating EA rainfall in this study. The EA region is under the direct influence of the Jet stream. As addressed in the previous sections, the variation of the Jet stream is closely connected with the MJO tropical forcing, EA meridional overturning circulation, and Rossby wave teleconnection. In this chapter, we show a comparative analysis of the MJO influences on EA rainfall based on the RMM and SVD indices.

doi:10.6342/NTU202303152

3.1 MJO-EA rainfall relationship based on RMM index

Most previous studies about EA weather and the MJO interactions emphasized the MJO heating in RMM phase 2–3 and phase 6–7 that are characterized by the dipole pattern centered at equatorial Indian Ocean and western Pacific as shown in Fig. 11b (e.g., Kim et al. 2006; Jeong et al. 2008; Jia et al. 2011; He et al. 2011), while relatively few (e.g., He et al. 2011; Song and Wu 2019) paid attentions to the heating in Maritime Continent area. Most of these previous studies examined the relation based on the phase-mean heating. Yet a look at the probability distribution of the EA rainfall in 8 phases of the MJO cycle based on RMM index (Fig. 15) reveals further important features. The figure confirms that while EA receives more rainfall in Phase 2–3, but nearly 50% chance of rain falls in Phase 8–1 when convection over MC is suppressed. A reversed probability distribution relation is seen in Phase 6–7 in Fig. 15. A composite rainfall and 850-hPa wind for the wet and dry days in Phase 2 (top and bottom 30% ranking) is shown in Fig. 16. Corresponding to dry and wet days in EA, the anomalous tropical rainfall shows a similar heating but significant differences in cooling east of Philippines and out of phase rainfall in EA.

To explore further, we show the composite rainfall and winds at 200-hPa for the EA wet days and dry days in a half MJO cycle through Phase 8, 1, 2, and 3 (Fig. 17). The Indian Ocean heating grows and propagates eastward in both groups, but the MJO tropical

doi:10.6342/NTU202303152

heating is only seen strongly coupled with the subtropical Rossby wave responses in the EA wet group. We also note in Fig. 17 that wet EA in RMM phase 8 and 1 mainly corresponds to a tropical cooling over MCWP. This is consistent with the analysis in He et al. (2011) who showed that a suppressed heating over MC and weaken local Hadley cell resulting in anomalous upward motion anomalies in the mid-latitude. We will show next the SVD index separates the EA wet day and dry days during the MJO cycle better than the RMM index does.

3.2 Comparison of MJO-EA rainfall relationship based on SVD and RMM index

We have demonstrated so far that the SVD index can better represent the Rossby wave responses to the MJO heating. In this chapter, we continue to investigate the influence of the MJO on winter rainfall over EA by the SVD index that we proposed in Chapter 2.

Here, we compare the composite fields of rainfall and 850-hPa winds for half MJO life cycle (S1, S2, S3, S4) defined by SVD2D_DJFM with the corresponding phases (P8, P1, P2, P3) by all-season RMM in Fig. 18. Notice again the one phase difference in the 8-phase life cycle by the two MJO index. The two half cycles show similar evolutions in the tropical rainfall distribution that features suppressed convection over MC in P8/S1, emerging convection over IO in P1/S2 and enhanced convection in P2–P3/S3–S4. The

doi:10.6342/NTU202303152

enhanced MJO convection in P2–P3/S3–S4 corresponds to anomalous rainfall in EA that have been identified in the literature (e.g., Kim et al. 2006; Jeong et al. 2008; Jia et al. 2011). But a significant difference appears in S2 when EA rainfall is already quite evident while the corresponding composite in P1 has no signal. The difference in EA rainfall is associated with a more evident negative rainfall anomalies east of Philippines (Sub_PH) and accompanied anticyclonic southwestly flow toward the EA rainfall anomalies (Fig. 18d). Note that Sub_PH is a variability center in the leading mode of OLR in Fig. 1 and the dry anomalies over Sub_PH also appears in RMM P1 in the wet EA group (Fig. 17). The comparison here along with the results in Fig. 17 demonstrates the SV2D_DJFM a more useful MJO index than the all-season RMM in identifying the MJO influences on EA rainfall in the phase when the MJO heating develops large meridional asymmetry in MCWP. Note again that the SVD index resolves stronger subtropical Rossby wave responses to the MJO heating as described in Chapter 2.

The near zero phase-mean rainfall anomalies in EA rainfall in RMM phase P1 is a result of near equal dry and wet days in the RMM phase as revealed in the frequency distribution of EA rainfall anomalies in Fig. 15. For a comparison, we show the frequency distribution of EA rainfall anomalies based on SVD phases in Fig. 19. One can see the frequency change in a way more conspicuous and coherent through the MJO cycle compared with the distribution based on RMM. The largest difference between Fig. 19

doi:10.6342/NTU202303152

and Fig. 15 is in the SVD phase S2 and the corresponding RMM phase P1. The probability of EA wet days is above 75% in S2 but below 50% in P1. This explains why the phase-averaged rainfall anomaly in S2 is significantly positive but near zero in P1. Similarly, the probabilities of anomalous rainy days identified in S3–S4 are all above 75 % while those in P2–P3 are notably below 75%. The probability distribution of anomalous rainfall days in the opposite phase S6–S8 compared with that in P5–P7 show comparable probabilities but for negative anomalies. The above analysis demonstrates that the SVD2D_DJFM index is a better MJO index to differentiate the wet and dry conditions for EA region. This is also supported by a scatter plot in MJO phase diagram shown in Fig. 20, in which the daily EA rainfall anomalous values are plotted in the MJO phase diagram by dots (blue for positive and red for negative) of different sizes. Compare the more diverse rainfall distribution in different RMM phases (Fig. 20a), the wet and dry anomalies in SVD phases are more clearly separated by SVD PC2 (Fig. 20b), which represents IO-MCWP mode. MCWP is in convective condition when SVD PC2 < 0, corresponding to the half cycle of MJO in phases S1–S4. The opposite occurs in phases S5–S8.

3.3 The sensitivity of the MJO-EA rainfall relationship to MJO indices

To demonstrate the robustness of the MCWP heating in MJO-EA rainfall

doi:10.6342/NTU202303152

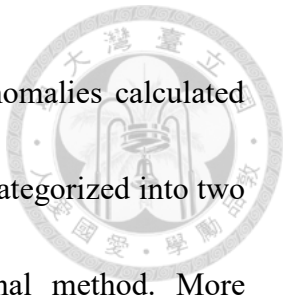

relationship, we show the probability distribution of EA rainfall anomalies calculated based on 6 selected MJO indices in Fig. 21. These 6 indices can be categorized into two groups as derived from 2-dimensional method and 1-dimensional method. More specifically, Figs. 21 a-d are the indices based on 2-dimensional data, including the SVD_U and the SVD_O from Chapter 2, the 25-90-day filtered OLR indices, and another SVD_U circulation index which was developed by using data only within 15°S-15°N. Figs. 21 e-f are for 1-dimensional indices, including the all-season RMM, the RMM_DJFM.

The sequence of the 8 MJO phases in Fig. 21 starts from RMM phase 8, when the suppressed convection locates over the Maritime Continent, and ends at RMM phase 7. For an easier comparison, MJO phases defined in each of the eight indices in Fig. 21 are arranged to follow the WH04 RMM phases so they all have similar spatial heating pattern. For example, the phase sequence of SVD_U index starts from its phase 1 (S1), for S1 is the phase with a similar spatial pattern as RMM phase 8 (P8). Further, phase composite maps for four selected MJO indices are presented in Fig. 22 in order to support this comparison. Notice that differences on the location of tropical heating still exists among indices, even though the phases have been adjusted to align with the WH04 RMM as the reference index.

General consistency of the modulation effect of the MJO on EA rainfall can be seen

doi:10.6342/NTU202303152

among the indices in Fig. 21. Basically, it shows the EA wet days appear during the first half MJO cycle (P8–P3/S1–S4) and the EA dry days during the second half (P4–P7/S5–S8). According to the SVD2D_DJFM index, S2–S4 (P1–P3) is identified as EA wet period, S6–S8 (P5–P7) is identified as EA dry period, and S1 (P8) and S5 (P4) are two transition periods, which show equal chance for EA wet and dry anomalies. This result is supported for all the 2-dimensional indices. For the other two 1-dimensional indices, their P1/S2 phase do not show enhanced rain (or more wet days) in EA. The composite OLR and wind in Fig. 22 further demonstrates the subtropical convection anomalies over east of Philippines (Sub_PH) as a key feature related to EA wetness. The 1-dimensional MJO indices are developed by longitudinal-averaged data that limits its ability to reveal the important Sub_PH heating.

Through Fig. 21 and Fig. 22, we summarize the importance of an MJO index to represent the evolution of the MJO heating in longitude and latitude and the associated extratropical responses.

3.4 The MCWP- and IO-heating and their associated circulation related to EA rainfall

Composite analysis for each MJO phase defined by SVD2D_DJFM index is performed to summarize the typical MJO-EA rainfall pattern. The EA wet (dry) cases for

doi:10.6342/NTU202303152

the composite are selected by the top (bottom) 1/3 of the frequency distribution of GPCP rainfall anomalies averaged over EA region. This is similar with what we have done by RMM index in Fig. 17. The series of typical wet EA-MJO connection pattern from S1–S5 are shown in Fig. 23. On the other hand, the series of dry EA-MJO connection pattern starting from S5 and ending at S1 are shown in Fig. 24. Both upper and lower level fields are shown for each phase by 2 sets of composite maps, including winds at 200-hPa and 850-hPa, height field at 200-hPa and 500-hPa, 850-hpa temperature as well as the GPCP rainfall anomalies.

In Fig. 23, we see S2 and S3 have the most significant EA rainfall. S2 is dominated by MCWP, while S3 is by a clear IO-MCWP dipole pattern. Both S2 and S3 show suppressed convection over the area east of Philippines (Sub_PH). On the other hand, no signals appear over Sub_PH in the EA dry composite from the bottom 1/3 cases in S2–S3 (not shown), which is consistent with the analysis by using RMM index (Fig. 17). The MCWP cooling with Sub_PH pattern is coupled with a significant baroclinic subtropical Rossby wave gyre, which bring southerly warm flow at the 850-hPa to the EA region, as well as establishing the meridional overturning flow that provide the favorable conditions for the EA rainfall. Furthermore, a large-scale significantly positive geopotential height anomalies (hereafter named Japan High) at 200-hPa and 500-hPa appear to the north of the cyclonic Rossby wave circulation associated with the MCWP cooling and form a

doi:10.6342/NTU202303152

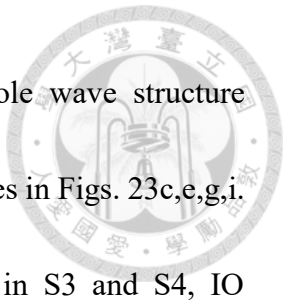

north-south dipole wave structure. Note that the north-south dipole wave structure evolves from S2 to S5 following the evolution of EA rainfall anomalies in Figs. 23c,e,g,i. When the EA north-south dipole wave structure is most evident in S3 and S4, IO convection is also most active. The convective heating causes anticyclonic Rossby wave at 200-hPa over IO and enhanced rainfall in EA as emphasized in previous studies (e.g., Kim et al. 2006; Jeong et al. 2008; Jia et al. 2011; Hung et al. 2014).

As S2 and S3 are the two phases with most significant EA wetness, S6 and S7 are the two phases with most significant EA dryness according the MJO phase defined by SVD2D_DJFM index. S6 and S7 can be regarded the opposite phase of S2 and S3 in general. On the connection with the tropical heating, the EA rainfall anomalies in S2 and S6 was related to a direct regional influence of the MCWP heating, while the EA rainfall anomalies in S3 and S7 was related to the IO-MWCP dipole heating that produces a remote and regional combined effect on extratropical responses in EA.

The Japan High is a key feature in the typical EA wet pattern (Fig. 23), but there is no comparable significant Japan Low shown in the typical EA dry pattern. Instead, the key feature at height fields in the typical EA dry pattern (Fig. 24) is positive anomalies over Asia at the upper layers (hereafter named Asia High). The occupation of the Asia High increase the chance for the low pressure or trough systems established or linger over the ocean east of EA, which favor the dry and northerly winter monsoon pattern as shown

doi:10.6342/NTU202303152

in S6–S7.

The above analysis shows MCWP heating play a more critical role than IO heating with regard to the MJO impact on EA rainfall. In the 8 phases of the MJO cycle, MCWP forcing is absent only in S4 and S8, which are the IO heating dominant phases in terms of Indo-western-Pacific region. S1, S2, S5, S6 are the phases dominated by MCWP forcing, when the IO convection is not yet developed or just begin to emerge. S2 and S6 has more robust MJO-EA rainfall relationship, while S1 and S5 are the transition phases, their MCWP forcing effect depends on the developing strength of the MWCP tropical heating. In other words, the emergence of EA weather depends on the successful establishment of the circulation coupled with the MCWP forcing over SUB_PH. Our study demonstrates that, except the forcing effect from the MJO's southward detour over MCWP (e.g., Kang et al. 2022), the existence of the suppressed heating over Sub_PH is also critical to the establishment of Rossby wave gyre and the overturning local Hadley cell circulation which connect the MJO tropical waves and EA weather.

doi:10.6342/NTU202303152

Chapter 4 The mechanism of MJO-EA rainfall relationship

We proceed to highlight the contrasting structure of the MJO heating and EA rain between S1-S2 and S3–S4. The analysis is shown in Chapter 4.1. We then examine in Chapter 4.2 the moisture budgets in the contrasting phases to show the sources of rainfall for EA rainfall. In Chapter 4.3, we perform modeling experiments to investigate the responsible mechanisms for the contrasting MJO heating and EA rainfall.

4.1 Analysis of MJO-EA rainfall relationship based on SVD mode 2

The distribution of anomalous daily EA rain in Fig. 20b shows that most wet days occur in SVD phases S2–S3–S4, dry days in S6–S7–S8, and transition days in S1 and S5. The figure further shows that most of the wet days occur when SVD PC2 $< -1\,\sigma$ (shaded in green). The above features lead us to focus on the dominant signals in SVD mode 2 defined by PC2 $< -1\,\sigma$ corresponding to S1–S4. The dominant SVD mode 2 is further divided into two groups: (PC2 $< -1\,\sigma$, PC1<0) and (PC2 $< -1\,\sigma$, PC1>0) that is referred to as SVD12 and SVD34, respectively.

The composite fields of anomalous GPCP rainfall and 200-hPa winds for SVD12 and SVD34 are shown in Fig. 25. We also show in Fig. 26 the composite anomalies of geopotential height at 500 hPa, temperature and winds at 850 hPa for SVD12 and SVD34. The structure of SVD12 (Figs. 25a and 26a) features suppressed convection over MCWP,

doi:10.6342/NTU202303152

warm and rainy weather in EA, cyclonic flow at 200-hPa and low pressure at 500-hPa in southeastern China and SCS. Convection over Indian Ocean has not yet developed in this stage. This is the pattern similar to a monopole heating in He et al. (2011) who referred it to as the MJO direct influence on EA through a local Hadley circulation effect. SVD34 is characterized by IO-MCWP dipole heating coupled with a wave train at 200-hPa consisting of anticyclonic flow over India and Indo-China and cyclonic flow over west Pacific along 25ºN (Fig. 25b). The wave train has long been recognized as the major pattern connecting the MJO and the EA rainfall. Figures 25 and 26 show that the coupling of MJO heating with circulation in SVD12 is mostly confined in East Asia and MCWP, while the MJO in SVD34 is associated with more active wave trains covering the whole Indo-Pacific sector.

The close link of the suppressed rainfall over MCWP, anticyclonic flow at 850 hPa and enhanced rainfall in EA in the composite fields for both SVD12 and SVD34 suggests that MCWP cooling weakens the meridional overturning circulation in East Asian winter monsoon between the MCWP divergent flow and the EA jet (e.g., Chang and Lau 1982; Chang et al. 2005). The resultant ascending motion together with the moisture advection from the anomalous southwesterly component of the MCWP divergent flow in the lower troposphere contribute to the EA rainfall system.

Although the anomalous southwesterly wind in SVD12 and SVD34 are all

doi:10.6342/NTU202303152

associated with MCWP divergent flow, the anomalous southwesterly component of the MCWP divergent flow in SVD34 is part of the forced Rossby wave gyre in response to the MJO dipole heating. This result suggests two mechanisms for the tropical MJO–EA rainfall relation: the MCWP monopole cooling in SVD12 and IO-MCWP dipole forcing in SVD34. Note that the anticyclonic flow and the suppressed convection over MCWP develops (in S1/S2) ahead of the IO heating (in S3/S4), suggesting the suppressed MCWP convection as the cause of weakened winter monsoon and the associated meridional moisture advection before the IO–MCWP heating-induced Rossby wave teleconnection becomes dominant.

4.2 Moisture budgets

The role of moisture supplies to the MJO has been emphasized by previous studies (e.g., Hsu and Li 2012; Tseng et al. 2015, and references therein). To show the contribution to the EA rainfall by moisture transport in the SVD12 versus SVD34, we calculate the vertically integrated moisture budget in the lower troposphere based on the following scale-separation of the moisture budget equation:

$$\partial_t q = -\boldsymbol{v} \cdot \nabla q - \omega \partial_p q - L^{-1} Q_2 \qquad (1)$$

The budget equation can be written in terms of basic and anomalous components (i.e. $q = \bar{q} + q'$, $\boldsymbol{v} = \overline{\boldsymbol{v}} + \boldsymbol{v}'$, $\omega = \bar{\omega} + \omega'$), and the difference of the Eq. (1) and the

doi:10.6342/NTU202303152

time mean of (1) gives

$$\partial_t q' = -\boldsymbol{v}' \cdot \nabla \bar{q} - \bar{\boldsymbol{v}} \cdot \nabla q' - \boldsymbol{v}' \cdot \nabla q' + \overline{\boldsymbol{v}' \cdot \nabla q'}$$
$$-\omega' \partial_p \bar{q} - \bar{\omega} \partial_p q' - \omega' \partial_p q' + \overline{\omega' \partial_p q'} - L^{-1}(Q_2 - \overline{Q_2}) \quad (2)$$

Then the phase composite of (2) can be written as

$$\partial_t \widetilde{q'} = -\widetilde{\boldsymbol{v}'} \cdot \nabla \bar{q} - \bar{\boldsymbol{v}} \cdot \nabla \widetilde{q'} - \widetilde{\boldsymbol{v}' \cdot \nabla} q' + \overline{\boldsymbol{v}' \cdot \nabla q'}$$
$$-\widetilde{\omega'} \partial_p \bar{q} - \bar{\omega} \partial_p \widetilde{q'} - \widetilde{\omega' \partial_p} q' + \overline{\omega' \partial_p q'} - L^{-1}(\widetilde{Q_2} - \overline{Q_2}) \quad (3)$$

We calculate the vertically integrated anomalous budgets (3)

$$Hadv = -\langle \widetilde{\boldsymbol{v}'} \cdot \nabla \bar{q} \rangle - \langle \bar{\boldsymbol{v}} \cdot \nabla \widetilde{q'} \rangle - \langle \widetilde{\boldsymbol{v}' \cdot \nabla} q' \rangle + \langle \overline{\boldsymbol{v}' \cdot \nabla q'} \rangle \quad (4)$$

$$Vadv = -\langle \widetilde{\omega'} \partial_p \bar{q} \rangle - \langle \bar{\omega} \partial_p \widetilde{q'} \rangle - \langle \omega' \widetilde{\partial_p q'} \rangle + \langle \overline{\omega' \partial_p q'} \rangle \quad (5)$$

$$R = -L^{-1}\left(\langle \widetilde{Q_2} \rangle - \overline{Q_2}\right) \quad (6)$$

where the angle bracket denotes vertical integration through four layers centered at 1000, 925, 850, and 700 hPa.

The composite budgets for the days corresponding to PC2<–1σ in SVD phase 1-4 (green shaded domain in Fig. 20b) in two groups PC1 < 0 and PC1 > 0 are shown in Fig. 27. In the group of SVD12, both horizontal and vertical moisture advection (Hadv in Fig. 27a and Vadv in Fig. 27c) show moistening in the EA region (marked by the rectangle) where enhanced rainfall consumes the moisture source. The advective moistening (Fig. 27a) supports the process by anomalous southwesterly component of the MCWP divergent flow to transport the moist air from tropical warm pool to EA region. The moisture budget for the group of SVD34 in Fig. 27b and Fig. 27d show similar features

doi:10.6342/NTU202303152

to that for SVD12, indicating the same advective processes are working. We further examine each component of the Hadv and Vadv in the scale separated budgets in (4) and (5). The results show that $-<\widetilde{\boldsymbol{v}'}\cdot\nabla\bar{q}>$ and $-<\widetilde{\omega'}\partial_p\bar{q}>$ are the dominant budget terms as shown in Fig. 28 for both SVD12 and SVD34. The overall distribution and magnitude of the budgets in Fig. 28 resemble those in Fig. 27, indicating that Hadv and Vadv are contributed primarily by advection of mean moisture field by intraseasonal flow $-<\widetilde{\boldsymbol{v}'}\cdot\nabla\bar{q}>$ and $-<\widetilde{\omega'}\partial_p\bar{q}>$, respectively, for both SVD12 and SVD34.

A more quantitative comparison of the budgets in the EA region (110ºE–150ºE, 20ºN–35ºN) is shown in Fig. 29. The budgets show a near balance between the anomalous advective moistening (of both the horizontal and vertical components) and condensation drying in both groups, and that total advective moistening in SVD12 (0.38 g $kg^{-1}day^{-1}$) is larger than that in SVD34 (0.29 g $kg^{-1}day^{-1}$). The budget further shows that the horizontal advection in SVD 12 (0.18 g $kg^{-1}day^{-1}$) is larger than that in SVD34 (0.09 g $kg^{-1}day^{-1}$), indicating a more significant role of the horizontal moisture advection in SVD12 than that in SVD34.

4.3 Forced experiments by a Linear Baroclinic Model

Previous studies have shown that the MJO-induced teleconnection is dominated by linear dynamics (e.g., Mori and Watanabe 2008; Tseng et al. 2019). Here we also use the

doi:10.6342/NTU202303152

linear baroclinic model (LBM) by Watanabe and Kimoto (2000) to examine the mechanisms of tropical–extratropical teleconnections discussed in Chapter 4.1. The model consists of primitive equations linearized about prescribed basic states. The vertical and horizontal resolutions of the model are 20 sigma levels and T42, respectively. Rayleigh friction and Newtonian cooling are employed in the model with an e-folding time of 20 days in most model layers except the top two layers and the bottom three layers where the e-folding time is 0.5 days. A fourth-order biharmonic damping (∇^4) with an e-folding time of 2 h is applied to damp the shortest wavenumber.

We perform experiments to simulate the phase-dependent teleconnection responses similar to the approach in Tseng et al. (2019). The model basic states are derived from the European Centre for Medium-Range Weather Forecasts (ECMWF) third-generation reanalysis product (ERA-Interim; Dee et al. 2011) by temporally averaging fields of variable during the extended boreal winter (November to March) from 1979 to 2015. The daily mean apparent heat source Q_1 defined by Yanai et al. (1973) is used to representing the MJO forcing.

$$Q_1 = \partial_t s + v \cdot \nabla s + \omega \partial_p s \tag{7}$$

The s defined by dry static energy ($s = c_p T + gz$) is used to representing the MJO forcing. The term Q_1 represents a collective effect of radiative cooling and subgrid-scale processes including condensation heating, evaporation, and eddy heat flux convergence.

doi:10.6342/NTU202303152

The anomalous Q_1 is derived by removing the first three harmonics of the seasonal cycle.

We conduct three experiments to test the teleconnection response to the variations of the MJO forcing. The first two experiments use the composite $Q_1' = \tilde{Q}_1 - \bar{Q}_1$ corresponding to SVD12 and SVD34, respectively. To further examine the forced response to negative heating in MCWP, we perform another experiment by imposing the same composite Q_1' as in SVD12 except within the area 110ºE–160ºE with negative heating only (hereafter referred to as MCWP). To ensure only tropical forcing is considered, only Q_1' within (20ºS–20ºN) is imposed in all three experiments.

The spatial distribution of Q_1' imposed in the three experiments is shown in Fig. 30 by the horizontal fields of vertically integrated Q_1' (Figs. 30a,b,c) and the vertical-zonal distribution of latitudinally averaged Q_1' within the tropical belt (15ºS–15ºN) (Figs. 30d,e,f). The vertically integrated Q_1' for SVD12 (Fig. 30a) and SVD34 (Fig. 30c) resembles the composite GPCP rainfall anomalies in Fig. 25a and Fig. 25b as expected because of the same days for the MJO composite. The vertical distribution of Q_1' for SVD12 and SVD34 (Figs. 30d,f) is characterized by deep anomalous heating profiles with peak values centered around 300–400-hPa layer where maximum cooling and heating reach −1.5 and 1K day^{-1}, respectively. The derivation of the heating (Q_1') and the spatial distribution of Q_1' for the three experiments are summarized in Table 1.

The LBM responses to the imposed tropical heating in the three experiments show

doi:10.6342/NTU202303152

a general pattern of a fast growth rate in the first pentad, a slower growth in the second pentad, and a quasi-steady state in the third pentad. For brevity, we choose to only show model responses at day 15 when the simulated fields are representative of the responses in the third pentad. The simulated horizontal winds and height fields at 900 and 230 hPa and vertical *p* velocity at 550 hPa for the three experiments SVD12, MCWP, and SVD34 are shown in Fig. 31, Fig. 32, and Fig. 33, respectively. The overall responses in the three experiments consist of the forced tropical wave signals within 20°S and 20°N and extratropical responses in the East Asian jet region (EAJ). Here EAJ includes East Asia and western North Pacific. The wave signals are the pairs of positive (negative) height anomalies or anticyclonic (cyclonic) circulation associated with the MJO cooling (heating) in the lower troposphere and the pairs of reversed circulation in the upper troposphere as labeled by letters H and L for high and low centers in Figs. 31a,c, 32a,c, and 33a,c.

The extratropical responses in EAJ in the three experiments all show a similar meridional overturning circulation between MCWP and EAJ consisting of anomalous anticyclonic flow (positive height) over SCS–WP and the associated southwesterly winds from Indo-China through Taiwan to Japan in the lower troposphere (Figs. 31c, 32c, and 33c) and reversed flow in the upper troposphere (Figs. 31a, 32a, and 33a). Also notable in the extratropical responses in EAJ are the anomalous high in the northern Pacific centered at 45°N, 180° and the anomalous low in mainland China through the troposphere.

doi:10.6342/NTU202303152

This anomalous MCWP–EAJ teleconnection implies a weakened East Asian winter monsoon circulation system consisting of the Mongolian high, Aleutian low, East Asian jet, and northeasterly wind. The East Asian monsoon and MCWP convection are known to be closely coupled with each other (e.g., Chang and Lau 1982; Chang et al. 2005). In this study, we show such a coupled variability associated with the MJO convection in MCWP. The weakened winter monsoon develops along with ascending motion in midtroposphere extending from southeast China to Japan (Figs. 31b, 32b, and 33b). The ascending motion is resulted primarily from a strong advection of vorticity of the mean zonal jet ($-\partial^2\bar{u}/\partial^2 y$) by the meridional thermal wind ($\partial v'/\partial p$) as required in quasigeostrophic theory (e.g., Kim et al. 2006).

The LBM results support our interpretation of the observational analysis of the influence of the MJO induced cooling in MCWP on EA rainfall discussed in Chapter 4.1 and 4.2; that is, the MCWP cooling weakens the meridional overturning in East Asian winter monsoon, and the resultant ascending motion along with the meridional moisture advection in EA all contribute to enhanced rainfall. The model results further suggest that the MCWP cooling induced weakened meridional overturning circulation is a more direct cause of enhanced rainfall in EA than the IO heating (or the IO–MCWP heating dipole) induced Rossby wave teleconnection.

doi:10.6342/NTU202303152

Chapter 5 The effect of MCWP in the model prediction

The observational analysis and the model experiments in the previous chapters emphasized the importance of tropical MCWP in the MJO evolution. Since the phase of MCWP cooling precedes the IO heating, previous studies have shown that cooling over MCWP and East Indian Ocean favors the initiation of the MJO over Indian Ocean (e.g., Zhao et al. 2013; Kim et al. 2014; Takasuka and Satoh 2021) and bearing the sources of predictability on sub-seasonal time scales (e.g., Waliser et al. 2003; Kim et al. 2018). Therefore, we extend the study in this chapter to investigate the effect of MCWP cooling on prediction of MJO and its influences on EA rainfall. We perform such a study by examining the prediction skills for two types of MJOs: those with and without significant MCWP cooling. The National Centers for Environmental Prediction (NCEP) Climate Forecasting System, version 2 (CFSv2; Saha et al. 2014) forecast model is used here to examine the effect of MCWP heating in the model prediction.

The definition, case selection, and comparative analysis for the two groups of MJO are described in Chapter 5.1. An assessment of the model prediction is shown in Chapter 5.2.

5.1 Cases selection and the observational analysis

The two leading PCs from the EOF analysis of 25–90-day filtered OLR of extended

doi:10.6342/NTU202303152

winter (December to March, DJFM) (see Fig. 1 in Chapter 2.1) are used for selecting and dividing Intraseasonal Oscillations (ISO) into 2 groups. Following the RMM index, we plot pairs of PC1 and PC2 corresponding to all daily OLR fields in the phase diagram with PC1 in x coordinate and PC2 in y coordinate. Those ISO events with significant MCWP cooling and IO-MCWP dipole heating (S12 and S34, amplitude $>1\sigma$) are selected as group A (ISO-A), PC1 remain negative during the 15 days before Day 0 of minimum PC2 (or peak IO convection). ISOs in group B (ISO-B) are similarly defined but without a precursory dry condition over Maritime Continent, i.e. no significant MCWP cooling phase (S12). We have identified 19 ISO-A and 12 ISO-B events during the period of 1998-2015.

The evolution in PC1 and PC2 of these events from day –20 to day +20 is shown in Fig. 34, both ISO-A and ISO-B has the minimum negative PC2 value at Day 0 of the ISO cycle. For the period of day -15 to day 0, the ISO-A events show stronger amplitude (greater than 1σ) while the ISO-B events show weak signal. After day 0, some ISO-B events appear to last longer with stronger amplitude than most ISO-A events. Figure 35 provides the composite evolution of averaged tropical rainfall (15°S to 15°N using CMORPH data) in time (day -20 to day 20) and longitude (80°E—180°E) for the two types of ISO. Both groups show IO-wet and WP-dry dipole pattern within day –3 and day +3, but significant differences in overall propagation. The ISO-A shows a clear

doi:10.6342/NTU202303152

propagation in dry phase from IO to WP during day -20 and day 0, and a following eastward propagation of wet phase from IO to WP during day 0 and day +20. The eastward propagating rainfall dissipates near MC around day +10 but redevelops over WP afterward. On the contrary, the ISO-B possess no propogating dry phase before day 0 but more significant and continuous eastward propagating wet phase during day 0 and day +20.

To reveal the evolution of spatial patterns of circulation and rainfall for ISO-A and ISO-B events, we show composite maps of rainfall, 200-hPa height, and 850-hPa winds for day -10, -5, 0, +5 in Fig. 36, and time-latitude cross-section of rainfall and circulation within 110°E-120°E within 15°N~30°N and day -20~day 20 in Fig. 37. The two figures show that the ISO circulation and the EA rainfall evolve in a more systematic way in ISO-A events than ISO-B events. The evolution of the ISO-A events resembles the typical MJO-EA relationship we describe in Chapter 3, those key features including the significant MCWP cooling, cyclonic(anticyclonic) flow at 200-hPa (850-hPa), and low-level southerly flow, enhanced EA rainfall at day -10 and -5 (Figs. 36a,b) are mostly consistent with the anomalous EA overturning circulation in phase SVD12 discussed in Chapter 3 and 4 (Figs. 25, 26 and 31). The following evolution of tropical rainfall dipole and associated subtropical Rossby wave train from day 0 to day +5 (Figs. 36c,d) also resembles those of SVD34 (Figs. 25, 26 and 33).

doi:10.6342/NTU202303152

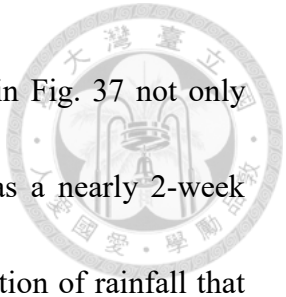

The time-latitude cross-section focus on EA longitude shown in Fig. 37 not only supports the above results, it also reveals that the ISO-A group has a nearly 2-week extended period of unstable weather over EA with continuous evolution of rainfall that emerges around 25°-30°N from about day -8, and moves southward to 20°N by day 10. The southward movement of the EA wetness after day0 is associated with the strengthening southwesterly flow near 15°-25°N. Both upper-level trough (or the cyclonic flow) and lower-level southwesterly flow contribute to the extended wet period, the associated circulation is related to the eastward-moving tropical heating of the MJO as discussed in previous chapters.

The above comparative analysis reveals that, relative to ISO-B events without a MCWP cooling phase, the ISO-A events with a leading MCWP phase evolve more systematically and bring a longer period of rain in East Asia. We address in the next sub-section their prediction skills.

5.2 Comparison in model prediction

Current MJO forecast skills are roughly limited to 4 weeks (e.g., Vitart et al. 2017). The model performance of MJO prediction is also known to be dependent on season, phase, as well as the initial MJO amplitude (e.g. Zhang and van den Dool 2012; H. Kim et al. 2014; Wang et al. 2014). Here, we would like to see if the model predicts ISO-A

doi:10.6342/NTU202303152

events differently from the ISO-B events.

The NCEP CFSv2, one of the widely used operational S2S forecast model, is adopted to conduct the comparison. The 45-day forecast data are first collected from 1998 to 2015, then we use the identified 19 ISO-A and 12 ISO-B MJO cases to make the composite mean for the two groups and compare their model forecast skill in different lead time. The examination focuses on two aspects similar to the observational analysis, the first is to check model performance on predicting the MJO equatorial eastward propagating, the second focus is on the MJO associated circulation and rainfall responses over near coastal East Asia.

On the propagation of tropical rainfall anomalies and 850-hPa zonal wind anomalies averaged over 15ºS–15ºN, Figure 38 shows the model forecasts for ISO-A and ISO-B at lead time 8day, 16day, 24day and 32day (Figs. 38b,c,d,e for ISO-A and Figs. 38g,h,i,j for ISO-B). This is similar to Fig. 35 for the observational analysis (shown in Fig. 38a for ISO-A and Fig. 38f). The model performance can be evaluated by the pattern correlation between the observed time-longitude evolution and predicted evolution at different lead times from day 0 to day 45 as shown in Fig. 39. The correlation in Fig. 39 shows the prediction of ISO-A events have higher skill than ISO-B events in the CFSv2 forecasts. For lead time within 10 days, the correlation for ISO-A is above 0.7, while correlation for ISO-B drops quickly down to 0.6 at lead time day 10. The model prediction skill in terms

doi:10.6342/NTU202303152

of correlation coefficient for ISO-A events remains higher than 0.5 for about 3 weeks, while the prediction skill for ISO-B events is about 2 weeks. A closer look at the prediction by the CFSv2 model (correlation > 0.5) for ISO-A and ISO-B at shorter lead time, e.g. day 8 in Fig. 38b and Fig. 38g, respectively, show an overall eastward propagating in tropical zonal wind and precipitation anomalies. Nevertheless, the model prediction exhibits a notable delay. For example, the observed IO-MCWP dipole in ISO-A events at Day0 (Fig. 38a) is predicted at +5 day and +15 day in the prediction at lead time 8-day (Fig. 38b) and 24-day (Fig. 38d). This delay is a notable forecast bias and is consistent with Wang (2014) who examined the MJO prediction in the NCEP CFSv2 and found the MJO propagation in CFSv2 too slow. Even with this model bias, the propagation of the dry mode along with the associated easterly wind anomalies from IO to WP in ISO-A events are well captured even at longer lead time at week 3-4 (Figs. 38c,d,e).

As for the model forecast performance on coastal East Asia (110°E-120°E), Figure 40 shows the model forecasts for ISO-A and ISO-B at lead time 8day, 16day, 24day and 32day (Figs. 40b,c,d,e for ISO-A and Figs. 40g,h,i,j for ISO-B) for the time-latitude cross-section over 15°N-30°N. The observed evolution for the two types of ISO is shown in Fig. 40a and Fig. 40f. The comparison again shows that the model performs better in predicting ISO-A cases than ISO-B cases. Specifically, the longer EA rain and associated

doi:10.6342/NTU202303152

high-level trough anomalies in ISO-A events (Fig. 40a) are predicted at various lead times (Figs. 40b,c,d,e). This may support our conclusion that MCWP cooling/heating is an important component of the MJO forcing that directly influence the EA rainfall. The result also supports previous studies that the precursory MCWP cooling and associated circulation favors the MJO initiation over Indian Ocean that is more predictable than those ISO events without the precursory signals.

doi:10.6342/NTU202303152

Chapter 6 Summary

This study focusses on influences of the MJO on East Asia rainfall in boreal winter. For such a regional impact study, the seasonal-dependent meridional structure of the MJO convection and associated subtropical franking Rossby waves are important features. Therefore, we develop an SVD2D_DJFM index based on 2-dimentional fields instead of the meridionally averaged 1-dimensional series as in RMM index, to resolve the seasonal spatial distribution of MJO tropical heating as well as the associated circulation structure. Considering the important influences of the mean state on the tropical wave responses to convection heating, we follow the bimodal MJO modes as in Kikuchi et al. (2012) by designing the SVD_DJFM index for the extended winter season. A similar SVD index can be defined for the boreal summer season.

The analysis based on SVD modes identifies the two leading modes of the wintertime MJO heating that are characterized by IOMC-CP and IO-MCWP dipole patterns. While similar dipole heating modes appear in other winter-based seasonal dependent MJO indices, such as 25-90-day filtered OLR and RMM_DJFM, our research emphasizes that EA rainfall anomalies are associated with the IO-MCWP leading mode, particularly the MJO heating variation over MCWP. Many previous studies based on RMM index found that East Asian winter rainfall is related to active convection in the Indian Ocean.

doi:10.6342/NTU202303152

Compared with the all-season RMM index, the SVD2D_DJFM index resolves stronger subtropical Rossby wave responses to the MJO heating. Also, the frequency distribution of EA rainfall anomalies based on SVD2D changes in a way more conspicuous and coherent through the MJO cycle. In particular, the SVD analysis identifies the convection anomalies over MCWP as a major cause of enhanced rainfall in EA at RMM phases 8 and 1 (SVD phase S1–S2). This is at least one-eighth of a cycle earlier than the phases of convection development over the Indian Ocean (IO). Our research shows that the MCWP cooling is as important as the IO heating in the MJO phase (RMM P2–P3/SVD S3–S4) that was regarded the major cause of EA rainfall in most previous studies (e.g., Kim et al. 2006; Jeong et al. 2008; Jia et al. 2011).

Our observational analysis on MJO heating and EA rainfall suggests that the cooling and heating in MCWP, either in the form of monopole or dipole mode, is an important component of the MJO through the life cycle. The analysis has further been substantiated in LBM experiments that reveal the unique role of cooling and heating over MCWP in the MJO influences on EA weather, i.e. the MCWP cooling drives a meridional overturning circulation in East Asia that interact with the East Asian Jet, which leads to an overall weakened East Asian monsoon system. This model result supports the interpretation of the observational analysis, in that the MCWP-cooling induced anomalous meridional circulation is a more direct cause of enhanced EA rainfall than the

doi:10.6342/NTU202303152

IO-heating (or the IO-MCWP heating dipole) induced Rossby wave teleconnection.

This study also points out a secondary center east of the Philippines (Sub_PH) located adjacent to the East Asian winter rainfall region is a critical component of the MJO–EA winter rainfall relationship. It appears that a broader cooling MCWP extending northward including Sub_PH tends to be coupled with significant baroclinic subtropical Rossby wave gyres, which bring low-level southerly warm flow to the EA region, as well as establishing the local Hadley overturning circulation inducing from the MCWP cooling that all provide the favorable conditions for the EA rainfall.

The important role of MCWP tropical forcing in the MJO cycle is further revealed in the prediction model. Our analysis shows MJO events carrying strong convection over Indian Ocean with a precursory MCWP cooling is more predictable in CFSv2 model than those without the precursory cooling. Such MJO events evolve from S12 (MCWP cooling monopole heating) to S34 (IO-dominant dipole heating), which are the MJO phases with circulation favorable for EA rainfall, can provide a long period of rain days lasting 2 weeks over EA. The results highlight the important role of the MWCP tropical forcing in the extended weather forecasts.

doi:10.6342/NTU202303152

Reference

Adames, Á. F., and J. M. Wallace, 2014: Three-dimensional structure and evolution of the vertical velocity and divergence fields in the MJO. J. Atmos. Sci., 71, 4661–4681.

Becker, E. J., E. H. Berbery, and R. W. Higgins, 2011: Modulation of cold-season U.S. daily precipitation by the Madden–Julian oscillation. J. Climate, 24, 5157–5166.

Bretherton, C. S., C. Smith, and J. M. Wallace, 1992: An intercomparison of methods for finding coupled patterns in climate data. J. Climate,5, 541–560.

Cassou, C., 2008: Intraseasonal interaction between the Madden– Julian oscillation and the North Atlantic Oscillation. Nature, 455, 523–527.

Chang, C.-P., and K.-M. Lau, 1982: Short-term planetary-scale interactions over the tropics and midlatitude during northern winter. Part I: Contrasts between active and inactive periods. Mon. Wea. Rev., 110, 933–946.

——, P. A. Harr, and H. J. Chen, 2005: Synoptic disturbances over the equatorial South China Sea and western Maritime Continent during boreal winter. Mon. Wea. Rev., 133, 489–503.

Chen, Y. L., C. H. Sui, C. P. Chang, and K.C. Tseng, 2021: Effect of the MJO on East Asian winter rainfall as revealed by an SVD analysis. 566 J. Climate, 34, 9729-9746.

Dee, D. P., and Coauthors, 2011: The ERA-Interim reanalysis: Configuration and performance of the data assimilation system. Quart. J. Roy. Meteor. Soc., 137, 553–

doi:10.6342/NTU202303152

597.

Ferranti, L., T. N. Palmer, F. Molteni, and E. Klinker, 1990: Tropical–extratropical interaction associated with the 30–60 day oscillation and its impact on medium and extended range prediction. J. Atmos. Sci., 47, 2177–2199.

Gill, A. E., 1980: Some simple solutions for heat-induced tropical circulation. Quart. J. Roy. Meteor. Soc., 106, 447–462.

Gottschalck, J., and Coauthors, 2010: A framework for assessing operational Madden–Julian oscillation forecasts: A CLIVAR MJO Working Group project. Bull. Amer. Meteor. Soc., 91, 1247–1258.

He, J., H. Lin, and Z. Wu, 2011: Another look at influences of the Madden–Julian oscillation on the wintertime East Asian weather. J. Geophys. Res., 116, D03109.

Hoskins, B. J., and D. J. Karoly, 1981: The steady linear response of a spherical atmosphere to thermal and orographic forcing. *J. Atmos. Sci.*,**38,** 1179–1196.

Hsu, H.-H., 1996: Global view of the intraseasonal oscillation during northern winter. Journal of Climate, 9, 2386–2406.

Hsu, P.-C., and T. Li, 2012: Role of the boundary layer moisture asymmetry in causing the eastward propagation of the Madden–Julian oscillation. J. Climate, 25, 4914–4931.

Hung, C.-W., H.-J. Lin, H.-H. Hsu, 2014: Madden–Julian Oscillation and the Winter

doi:10.6342/NTU202303152

Rainfall in Taiwan. J. Clim. 27:12, 4521-4530.

Jeong, J.- H., B.- M. Kim, C.- H. Ho, and Y.- H. Noh, 2008: Systematic variation in wintertime precipitation in East Asia by MJO- induced extratropical vertical motion, J. Clim., 21, 788–801.

Jia, X., L. Chen, F. Ren, and C. Li, 2011: Impacts of the MJO on winter rainfall and circulation in China. Adv. Atmos. Sci., 28, 521–533, doi:10.1007/s00376-010-9118-z.

Jiang, X., and Coauthors, 2020: Fifty years of research on the Madden-Julian oscillation: Recent progress, challenges, and perspectives. J. Geophys. Res. Atmos., 125, e2019JD030911.

Jin, F., and B. J. Hoskins, 1995: The direct response to tropical heating in a baroclinic atmosphere. J. Atmos. Sci., 52, 307–319.

Jones, C., and L. M. Carvalho, 2012: Spatial–intensity variations in extreme precipitation in the contiguous United States and the Madden–Julian oscillation. J. Climate, 25, 4898–4913.

Kanamitsu, M., W. Ebisuzaki, J. Woollen, S.-K. Yang, J. J. Hnilo, M. Fiorino, and G. L. Potter, 2002: NCEP–DOE AMIP-II Reanalysis (R-2). Bull. Amer. Meteor. Soc., 83, 1631–1643.

Kang, D., D. Kim, S. Rushley, and E. D. Maloney, 2022: Seasonal locking of the MJO's

doi:10.6342/NTU202303152

southward detouring of the Maritime Continent: The role of the Australian monsoon. J. Climate, 35, 4553–4568.

Kikuchi, K., B. Wang, and Y. Kajikawa, 2012: Bimodal representation of the tropical intraseasonal oscillation. Climate Dyn., 38, 1989–2000.

Kiladis, G. N., K. H. Straub, and P. T. Haertel, 2005: Zonal and vertical structure of the Madden–Julian oscillation. J. Atmos. Sci., 62, 2790–2809.

Kim, B.-M., G.-H. Lim, and K.-Y. Kim, 2006: A new look at the midlatitude-MJO teleconnection in the northern hemisphere winter. Quart. J. Roy. Meteor. Soc., 132, 485–503.

Kim, D., J.-S. Kug, and A. H. Sobel, 2014: Propagating versus nonpropagating Madden–Julian oscillation events. J. Climate, 27, 111–125.

Kim, H.-M., P. J. Webster, V. E. Toma, and D. Kim, 2014: Predictability and prediction skill of the MJO in two operational forecasting systems. J. Climate, 27, 5364–5378.

Kim, H., Vitart, F., & Waliser, D. E. (2018). Prediction of the Madden-Julian Oscillation: A review. Journal of Climate, 31, 9425– 9443.

Lee, H.-T., and NOAA CDR Program, 2011: NOAA Climate Data Record (CDR) of Daily Outgoing Longwave Radiation (OLR), version 1.2. NOAA National Climatic Data Center.

Lee, J.-Y., B. Wang, M. C. Wheeler, X. Fu, D. E. Waliser, and I.-S. Kang, 2013: Real-

doi:10.6342/NTU202303152

time multivariate indices for the boreal summer intraseasonal oscillation over the Asian summer monsoon region. Climate Dyn., 40, 493–509.

Li, T., J. Ling, and P.-C. Hsu, 2020: Madden–Julian Oscillation: Its discovery, dynamics, and impact on East Asia. J. Meteor. Res., 34, 20–42.

Lin, H., G. Brunet, and J. Derome, 2009: An observed connection between the North Atlantic Oscillation and the Madden–Julian oscillation. J. Climate, 22, 364–380.

Lin, H., G. Brunet, and R. Mo, 2010: Impact of the Madden–Julian oscillation on wintertime precipitation in Canada. Mon. Wea. Rev., 138, 3822–3839,

Lin, H., 2022: The Madden-Julian oscillation. Atmosphere-Ocean. 60:3-4,338-359.

Ling, J., and Coauthors, 2017: Challenges and opportunities in MJO studies. Bull. Amer. Meteor. Soc., 98, ES53–ES56.

Madden, R. A., and P. R. Julian, 1971: Detection of a 40–50 day oscillation in the zonal wind in the tropical Pacific. J. Atmos. Sci., 28, 702–708.

Madden, R. A., and P. R. Julian, 1972: Description of global-scale circulation cells in the tropics with a 40–50 day period. J. Atmos. Sci., 29, 1109–1123.

Madden, R. A., and P. R. Julian, 1994: Observations of the 40–50-day tropical oscillation—A review. Mon. Wea. Rev., 122, 814–837.

Matthews, A. J., B. J. Hoskins, and M. Masutani, 2004: The global response to tropical heating in the Madden–Julian oscillation during the northern winter. Quart. J. Roy.

doi:10.6342/NTU202303152

Meteor. Soc., 130, 1991–2011..

Mo, K. C., and R. W. Higgins, 1998: Tropical convection and precipitation regimes in the western United States. J. Climate, 11, 2404–2423.

Mori, M., and M. Watanabe, 2008: The growth and triggering mechanisms of the PNA: A MJO–PNA coherence. J. Meteor. Soc. Japan, 86, 213–236.

Roundy, P. E., C. J. Schreck III, and M. A. Janiga, 2009: Contributions of convectively coupled equatorial Rossby waves and Kelvin waves to the real-time multivariate MJO indices. Mon. Wea. Rev., 137, 469–478.

Saha, S., and Coauthors, 2014: The NCEP Climate Forecast System version 2. J. Climate, 27, 2185–2208.

Schreck, C. J., H.-T. Lee, and K. R. Knapp, 2018: HIRS outgoing longwave radiation—daily climate data record: Application toward identifying tropical subseasonal variability. Remote Sens., 10, 1325.

Seo, K., and S. Son, 2012: The global atmospheric circulation response to tropical diabatic heating associated with the Madden–Julian oscillation during northern winter. J. Atmos. Sci., 69, 79–96.

Song, L., and R. Wu, 2019: Impacts of MJO convection over the maritime continent on Eastern China cold temperatures. J. Climate, 32, 3429–3449.

Simmons, A. J., J. M. Wallace, and G. W. Branstator, 1983: Barotropic wave propagation

doi:10.6342/NTU202303152

and instability, and atmospheric teleconnection patterns. J. Atmos. Sci., 40, 1363–1392.

Stan, C., D. M. Straus, J. S. Frederiksen, H. Lin, E. D. Maloney, and C. Schumacher, 2017: Review of tropical–extratropical teleconnections on intraseasonal time scales. Rev. Geophys., 55, 902–937.

Straub, K. H., 2013: MJO initiation in the real-time multivariate MJO index. J. Climate, 26, 1130–1151.

Takasuka, D., and M. Satoh, 2021: Diversity of the Madden–Julian oscillation: Initiation region modulated by the interaction between the intraseasonal and interannual variabilities. J. Climate, 34, 2297–2318.

Tseng, K.-C., C.-H. Sui, and T. Li, 2015: Moistening processes for Madden–Julian oscillations during DYNAMO/CINDY. J. Climate, 28, 3041–3058.

Tseng, K.-C., E. Maloney, and E. Barnes, 2019: The consistency of MJO teleconnection patterns: An explanation using linear Rossby wave theory. J. Climate, 32, 531–548.

Ventrice, M. J., M. C. Wheeler, H. H. Hendon, C. J. Schreck, C. D. Thorncroft, and G. N. Kiladis, 2013: A modified multivariate Madden–Julian oscillation index using velocity potential. Mon. Wea. Rev., 141, 4197–4210.

Vitart, F., and Coauthors, 2017: The Subseasonal to Seasonal (S2S) prediction project database. *Bull. Amer. Meteor. Soc.*, **98**, 163–173.

doi:10.6342/NTU202303152

Waliser, D. E., K. M. Lau, W. Stern, and C. Jones, 2003: Potential predictability of the Madden–Julian oscillation. *Bull. Amer. Meteor. Soc.*, **84**, 33–50, 5.1

Waliser, D. E. and K. R. Sperber, 2015: Filling a capability and decision support gap between weather and seasonal forecasts: The role of USCLIVAR and initiating efforts of its MJO Working Group. American Geophysical Union, Fall Meeting 2015, abstract id. PA51A-2199.

Wang, B., and H. Rui, 1990: Dynamics of the coupled moist Kelvin–Rossby wave on an equatorial β-plane. J. Atmos. Sci., 47, 397–413.

Wang, W., M.-P. Hung, S. J. Weaver, A. Kumar, and X. Fu, 2014: MJO prediction in the NCEP Climate Forecast System version 2. Climate Dyn., 42, 2509–2520.

Watanabe, M., and M. Kimoto, 2000: Atmosphere–ocean thermal coupling in the North Atlantic: A positive feedback. Quart. J. Roy. Meteor. Soc., 126, 3343–3369.

Wheeler, M. C., and H. H. Hendon, 2004: An all-season real-time multivariate MJO index: Development of an index for monitoring and prediction. Mon. Wea. Rev., 132, 1917–1932.

Wheeler, M. C., H. J. Kim, J. Y. Lee, and J. C. Gottschalck, 2017: Real-time forecasting of modes of tropical intraseasonal variability: The Madden–Julian and boreal summer intraseasonal oscillations. The Global Monsoon System: Research and Forecast, C.-P. Chang et al., Eds., World Scientific, 131–138.

doi:10.6342/NTU202303152

Xie, P., J. E. Janowiak, P. A. Arkin, R. Adler, A. Gruber, R. Ferraro, G. J. Huffman, and S. Curtis, 2003: GPCP pentad precipitation analyses: An experimental data set based on gauge observations and satellite estimates. J. Climate, 16, 2197–2214.

Yanai, M., S. Esbensen, and J.-H. Chu, 1973: Determination of bulk properties of tropical cloud clusters from large-scale heat and moisture budgets. J. Atmos. Sci., 30, 611–627.

Yao, Y., H. Lin, and Q. Wu, 2015: Subseasonal variability of precipitation in China during boreal winter. J. Climate, 28, 6548–655.

Zhang, C., 2005: Madden-Julian Oscillation. Rev. Geophys., 43, RG2003.

Zhang, C., 2013: Madden–Julian oscillation: Bridging weather and climate. Bull. Amer. Meteor. Soc., 94, 1849–1870.

Zheng, C., E. K. Chang, H.-M. Kim, and M. Zhang, 2018: Impacts of the Madden–Julian oscillation on storm-track activity, surface air temperature, and precipitation over North America. J. Climate, 31, 6113–6134.

Zheng, C., and E. K. M. Chang, 2019: The role of MJO propagation, lifetime, and intensity on modulating the temporal evolution of the MJO extratropical response. J. Geophys. Res., 124, 5352–5378.

Zheng, C., and E. K.-M. Chang, 2020: The role of extratropical background flow in modulating the MJO extratropical response. J. Climate, 33, 4513–4536.

doi:10.6342/NTU202303152

Zhang, Q., and H. van den Dool, 2012: Relative merit of model improvement versus availability of retrospective forecasts: The case of Climate Forecast System MJO prediction. Wea. Forecasting, 27, 1045–1051.

Zhao, C., T. Li, and T. Zhou, 2013: Precursor signals and processes associated with MJO initiation over the tropical Indian Ocean. J. Climate, 26, 291–307.

doi:10.6342/NTU202303152

Table 1 Summary of the derivation of the MJO heating (Q_1') and the spatial distribution of (Q_1') imposed in the three experiments.

Exp ID	Composite Q_1' in time (imposed area)	Spatial distribution of Q_1'
SVD12	MJO SVD phase 1-2, PC2 $< 1\sigma$ (20ºS-20ºN)	Figs. 30a,d
SVD34	MJO SVD phase 3-4, PC2 $< 1\sigma$ (20ºS-20ºN)	Figs. 30c,f
MCWP	MJO SVD phase 1-2, PC2 $< 1\sigma$ (20ºS-20ºN, 110º-160ºE, negative heating only)	Figs. 30b,e

doi:10.6342/NTU202303152

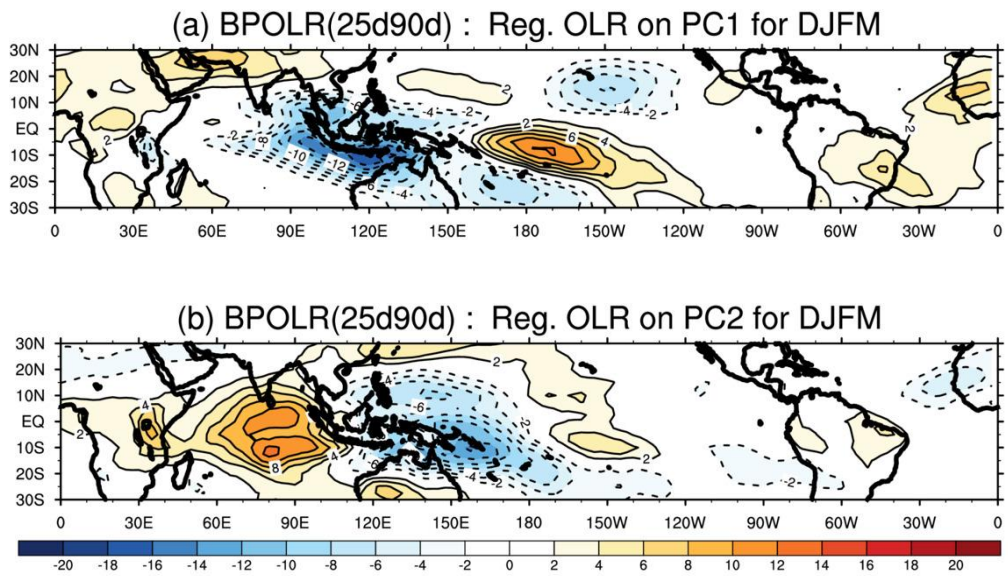

Figure 1 Regressed daily OLR anomalies (OLR′) onto the PC of (a) EOF1 and (b) EOF2 of 25–90-day filtered OLR for extended winter (December to March). Daily OLR′ is obtained by removing seasonal cycle and the previous 120-day mean.

doi:10.6342/NTU202303152

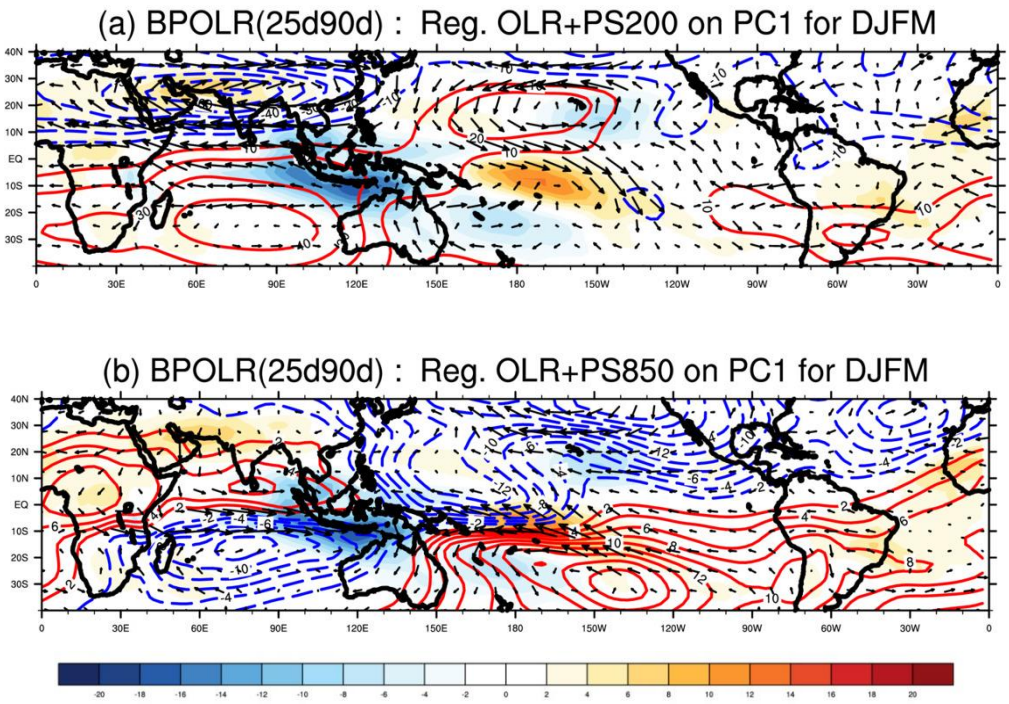

Figure 2 Regressed OLR, streamfunction (contours, unit: $10^{-6}m^2s^{-1}$) and vector wind at (a) 200-hPa and (b) 850-hPa, against the EOF1 of 25–90-day filtered OLR for extended winter (December to March).

doi:10.6342/NTU202303152

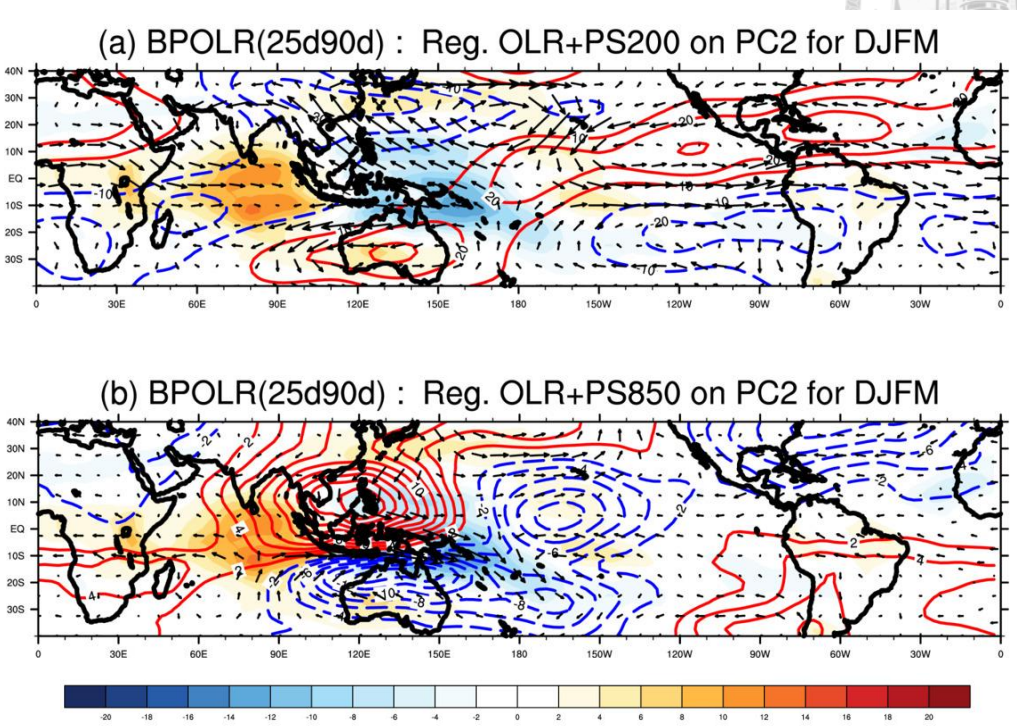

Figure 3 Same as Fig. 2, except for EOF2.

doi:10.6342/NTU202303152

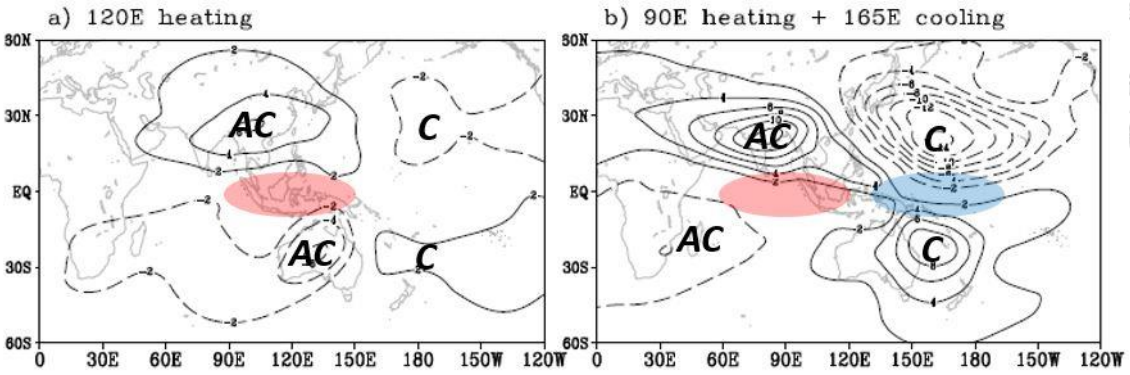

Figure 4 The simulated 200-hPa stream function at day 5 in response to four idealized heating (heating and cooling shaded in red and blue) in He et al. (2011): (a) H120 (b) H90C165.

doi:10.6342/NTU202303152

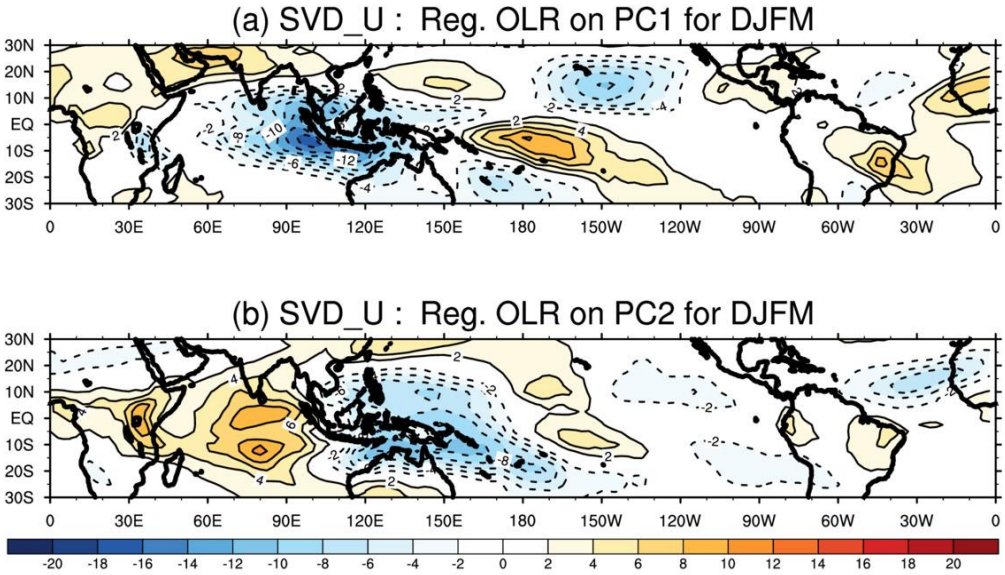

Figure 5 Same as Fig. 1, except for SVD_U index.

doi:10.6342/NTU202303152

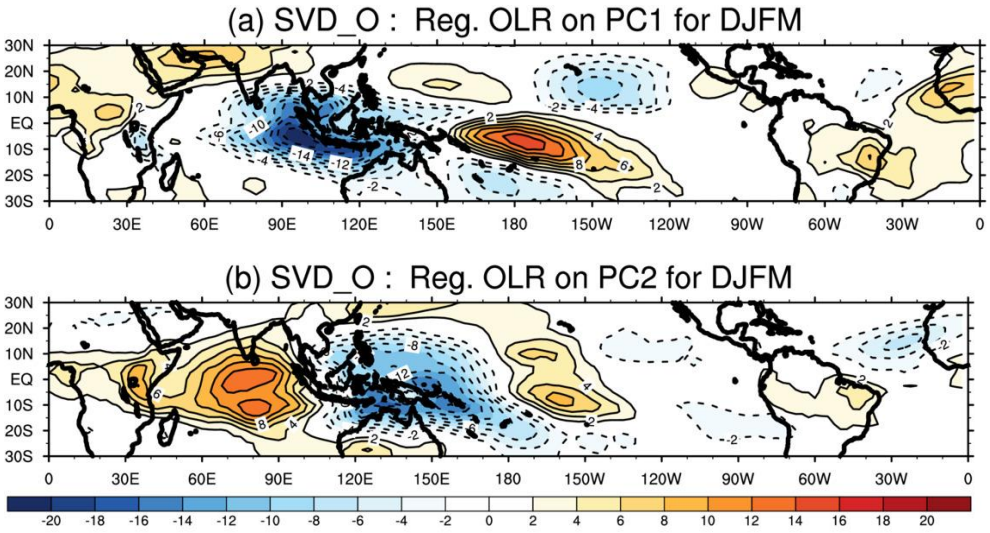

Figure 6 Same as Fig. 1, except for SVD_O index.

doi:10.6342/NTU202303152

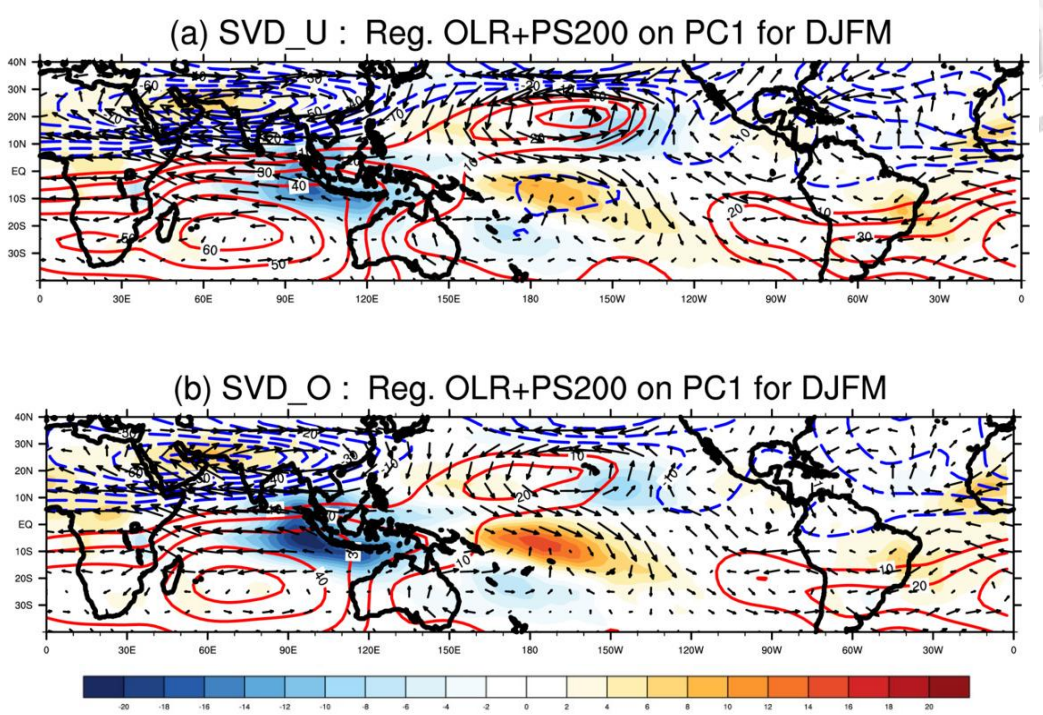

Figure 7 Regressed OLR, streamfunction (contours, unit: $10^{-6}m^2s^{-1}$) and vector wind at 200-hPa against EOF1 of (a) SVD_U, and (b) SVD_O index for extended winter (December to March).

doi:10.6342/NTU202303152

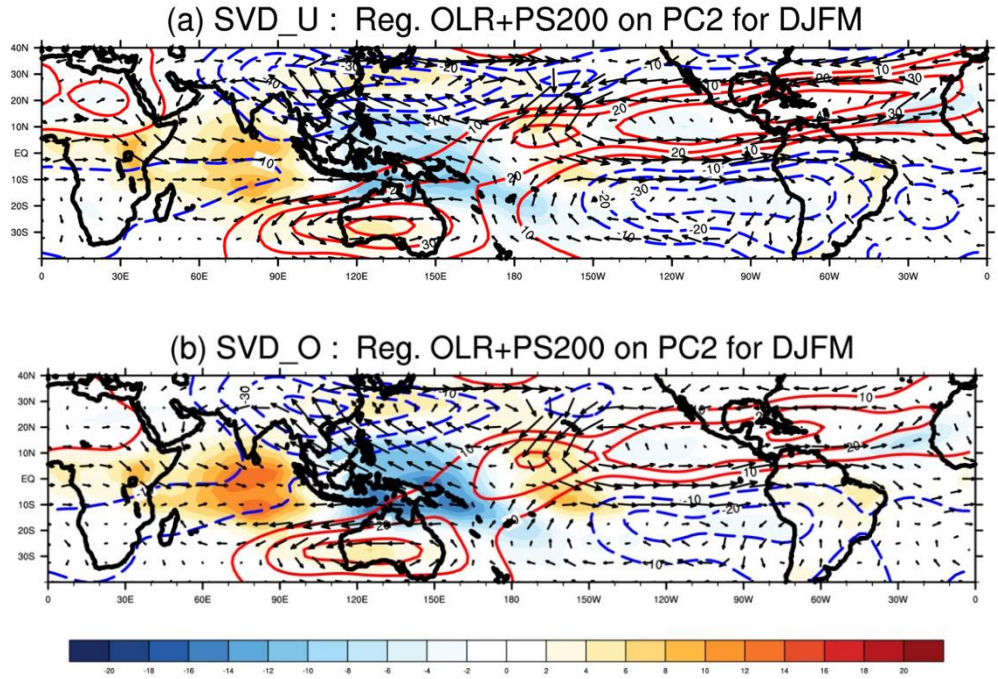

Figure 8 Same as Fig. 7, except for EOF2.

doi:10.6342/NTU202303152

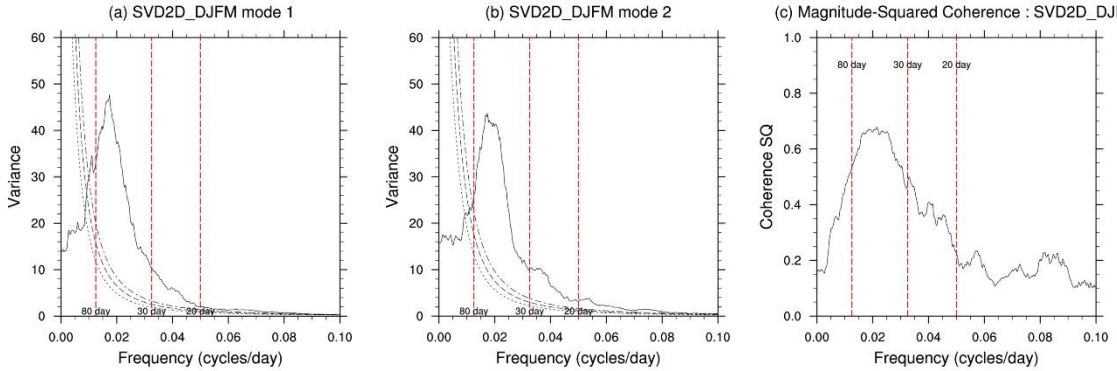

Figure 9　The power spectra of the reference time series of the (a) SVD_U mode 1, (b) SVD_U mode 2, and (c) their coherence square, derived from the SVD2D_DJFM analysis.

doi:10.6342/NTU202303152

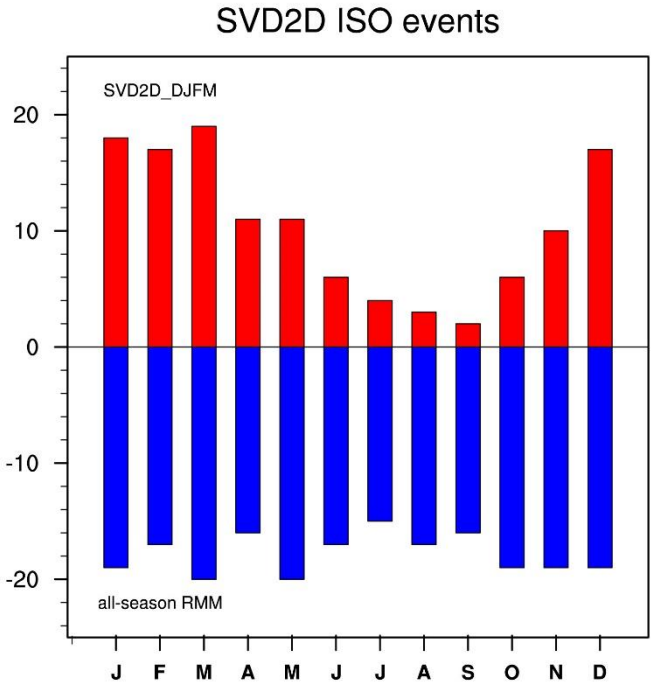

Figure 10　The average number of MJO days in each of the 12 calendar months, 1980–2015. The MJO days are defined by the amplitude of the MJO index, SVD2D_DJFM (red bars) and all-season RMM (blue bars), larger than > 1.

doi:10.6342/NTU202303152

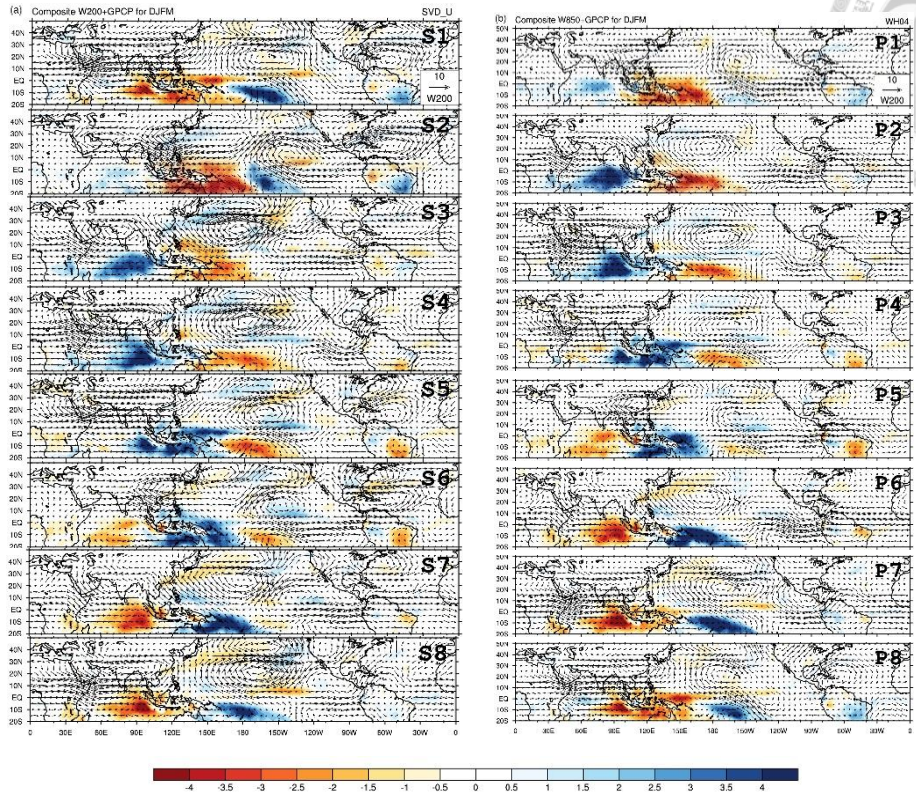

Figure 11　Composites of anomalous GPCP rainfall and winds at 200-hPa (black arrow) for 8 MJO phases based on (a) SVD2D_DJFM index and (b) RMM index.

doi:10.6342/NTU202303152

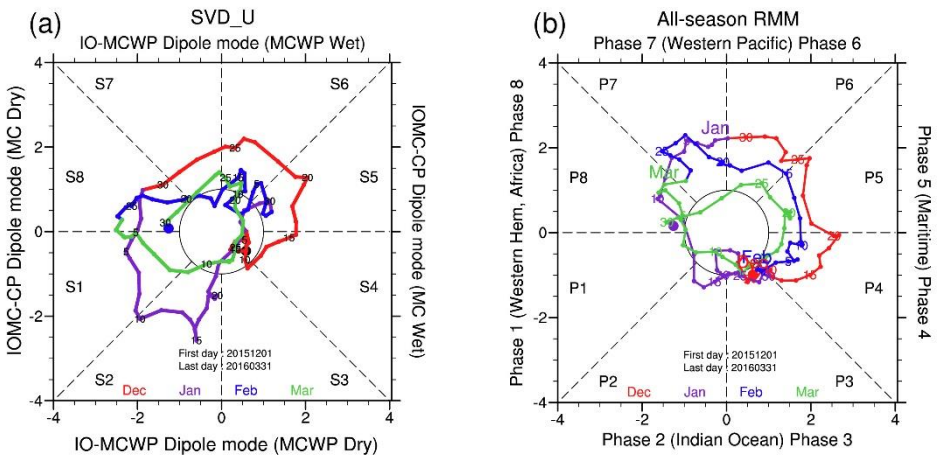

Figure 12 MJO phase diagram based on (a) SVD_U index and (b) all-season RMM index for a winter season from December 2015 to March 2016 when two successive MJOs occurred.

doi:10.6342/NTU202303152

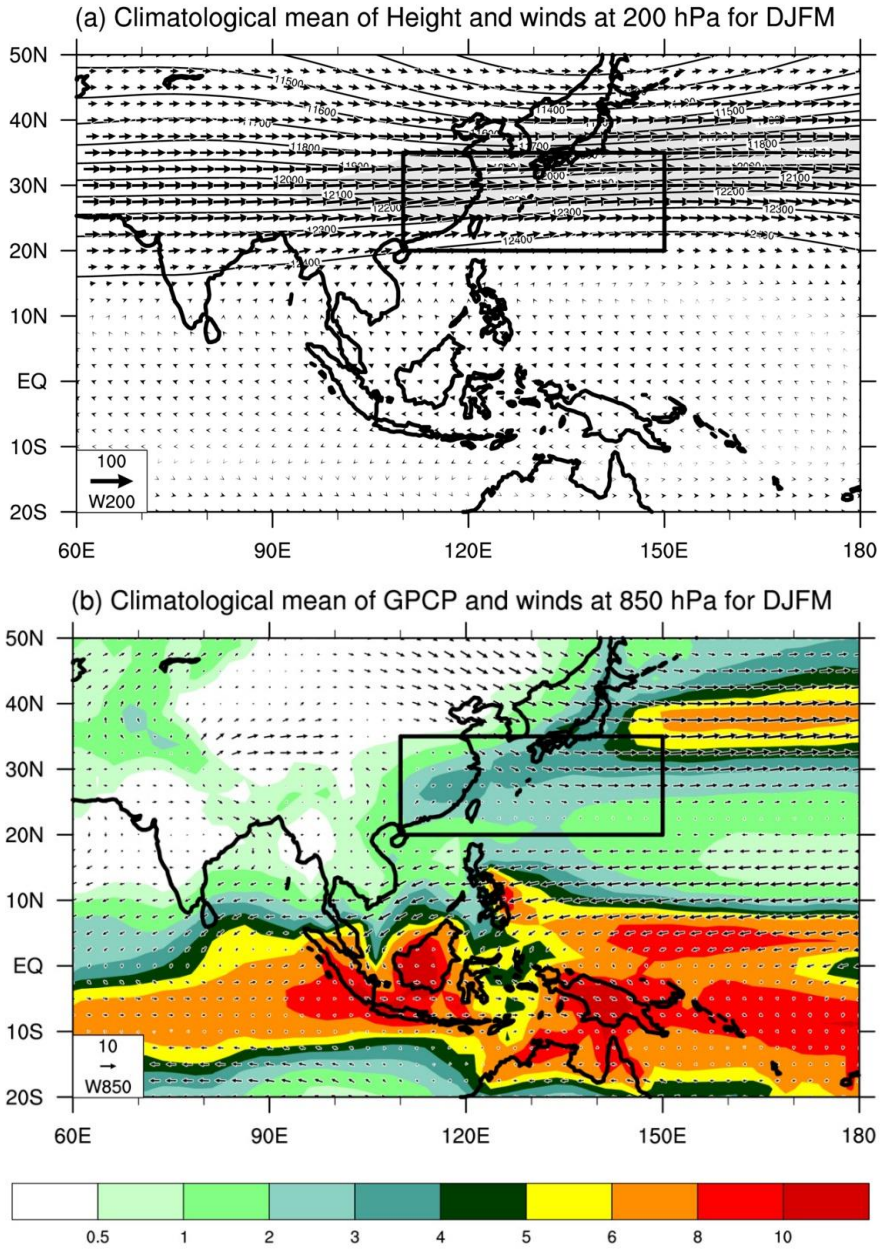

Figure 13 Climatological mean of (a) Height (contour), (u, v), and wind speed (light shadings) at 200-hPa; (b) (u, v) at 850-hPa and GPCP precipitation for extended winter season (DJFM) based on 1980–2015.

doi:10.6342/NTU202303152

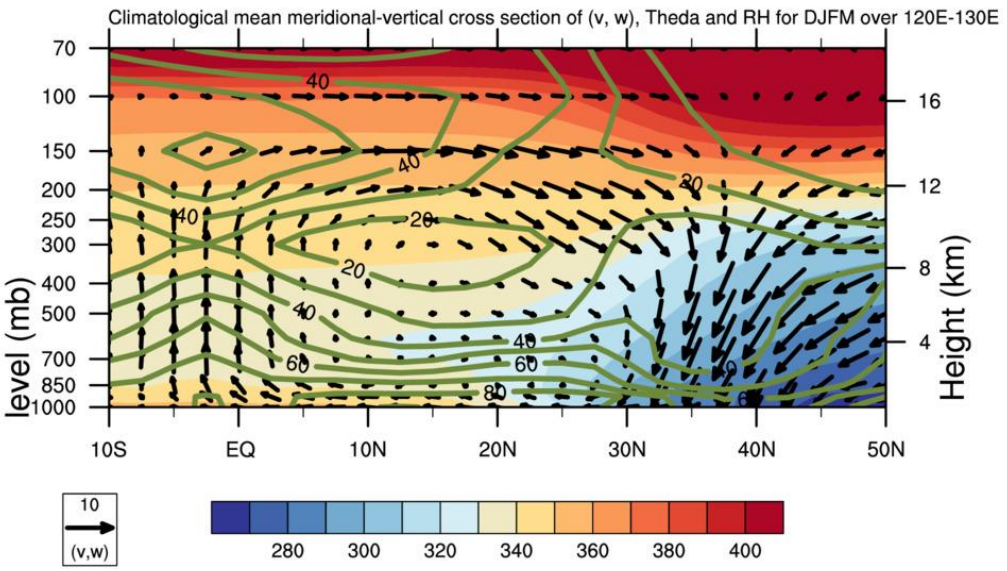

Figure 14 Climatological mean meridional-vertical cross section of (v, w), potential temperature (colored), and relative humidity (contoured in green) within 120°-130°E for extended winter season (DJFM) based on 1980–2015.

doi:10.6342/NTU202303152

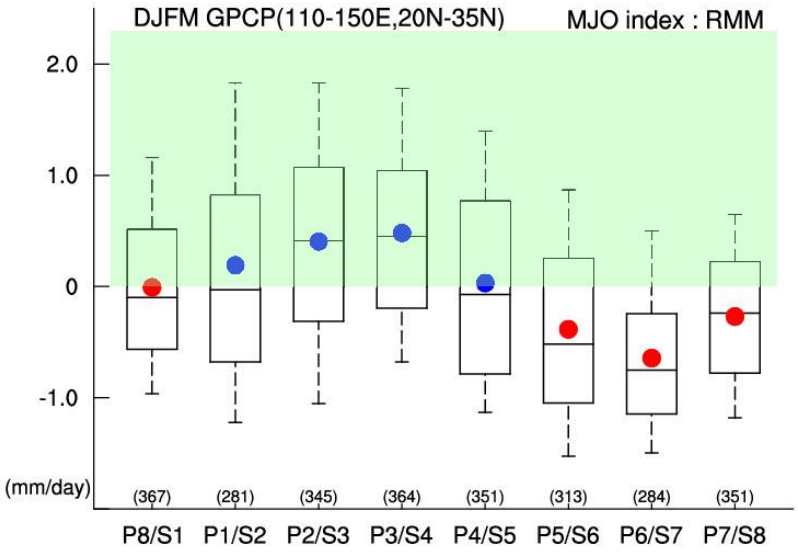

Figure 15 Probability distribution of rainfall anomalies within the EA region in the 8 phases of the MJO defined by all-season RMM index.

doi:10.6342/NTU202303152

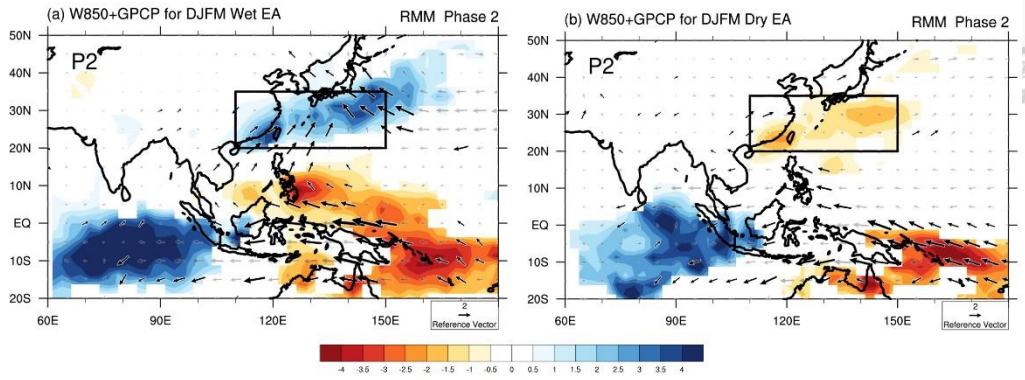

Figure 16 Composites of anomalous GPCP rainfall and winds at 850-hPa in RMM Phase 2 for (a) top 1/3 and (b) bottom 1/3 of days sorted out by the frequency distribution of GPCP rainfall anomalies averaged in East Asian region marked by the black rectangle.

doi:10.6342/NTU202303152

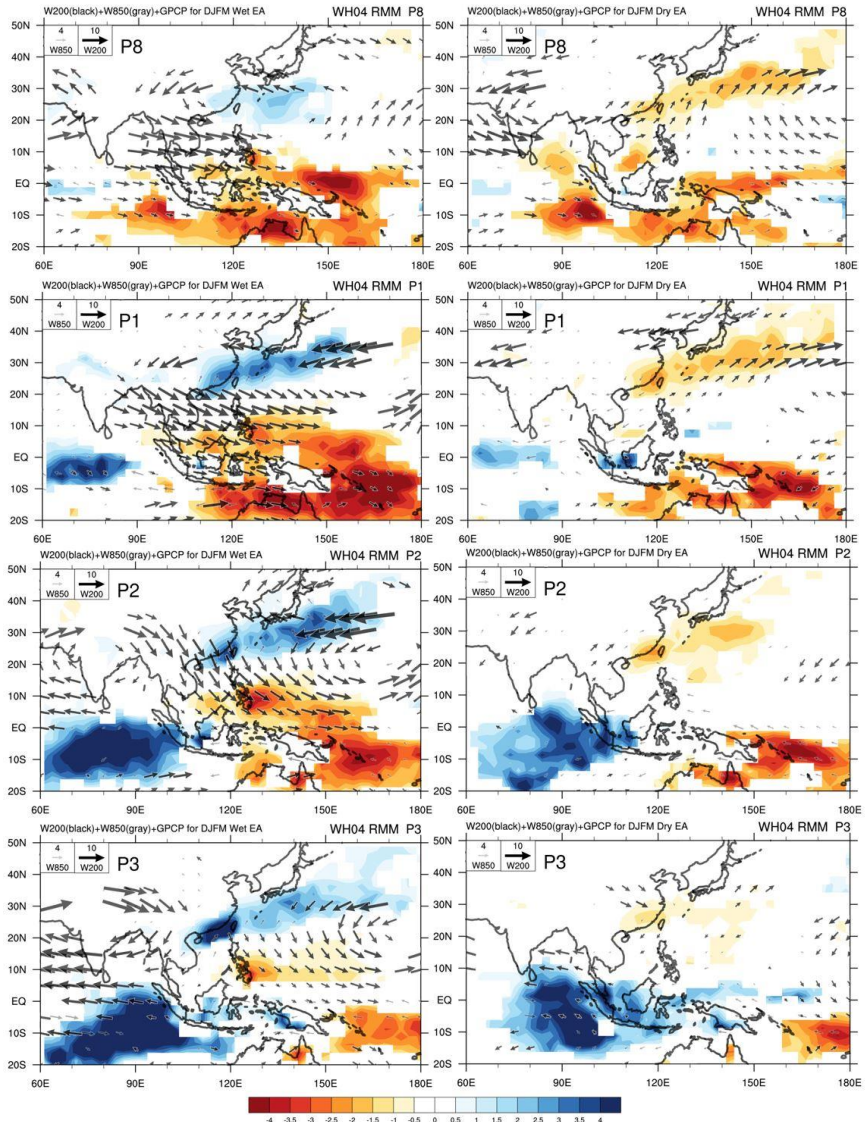

Figure 17　Composites of anomalous GPCP rainfall and winds at 850-hPa (gray arrow) and 200-hPa (black arrow) in RMM Phase 8-1-2-3 for top 1/3(Left) and bottom 1/3(Right) of days arranged by the frequency distribution of averaged GPCP rainfall anomalies in East Asian rainfall region.

doi:10.6342/NTU202303152

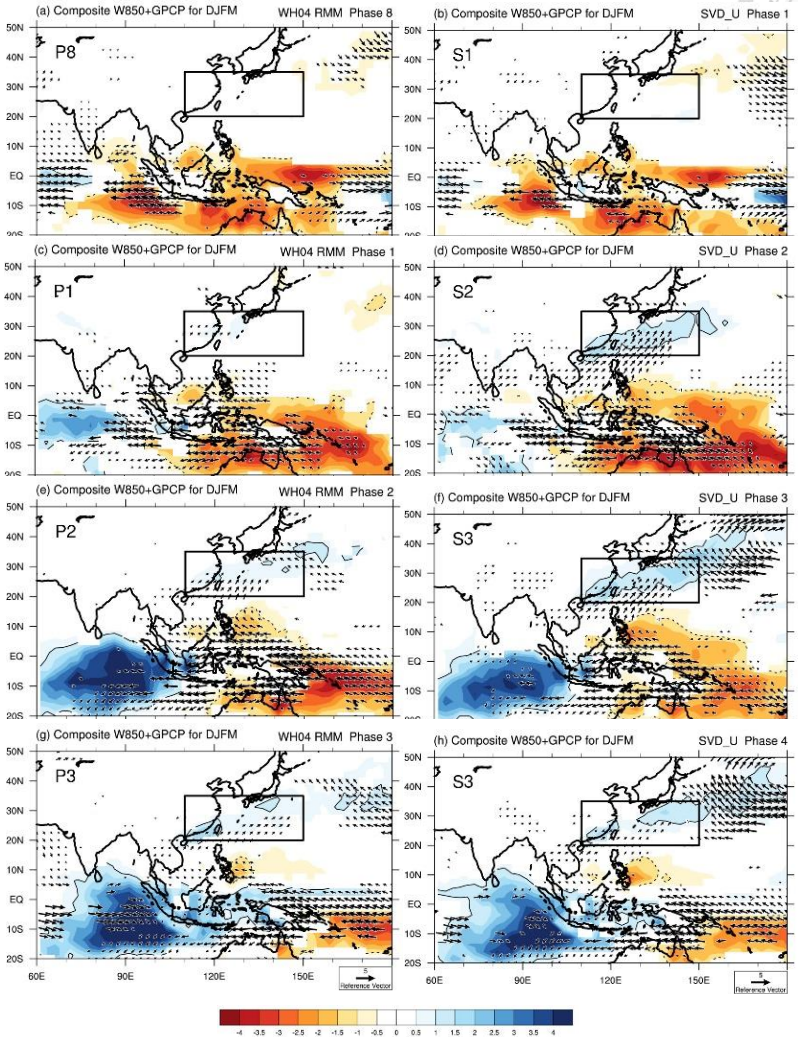

Figure 18 Composite fields of anomalous GPCP rainfall and 850-hPa wind for the half cycle of the MJO (P8, P1, P2, P3) defined by all-season RMM and (S1, S2, S3, S4) by SVD2D_DJFM. The composite fields are shown in the order of four phases (a, b) P8, S1, (c, d) P1, S2, (e, f) P2, S3, (g, h) P3, S4. The unit of GPCP and wind is mm day^{-1} and m s^{-1}.

doi:10.6342/NTU202303152

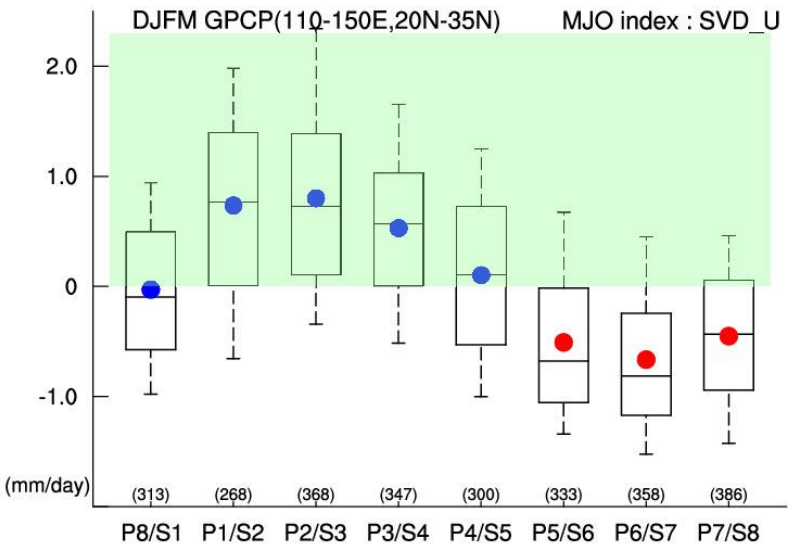

Figure 19　Probability distribution of rainfall anomalies within the EA region in the 8 phases of MJO defined by SVD index.

doi:10.6342/NTU202303152

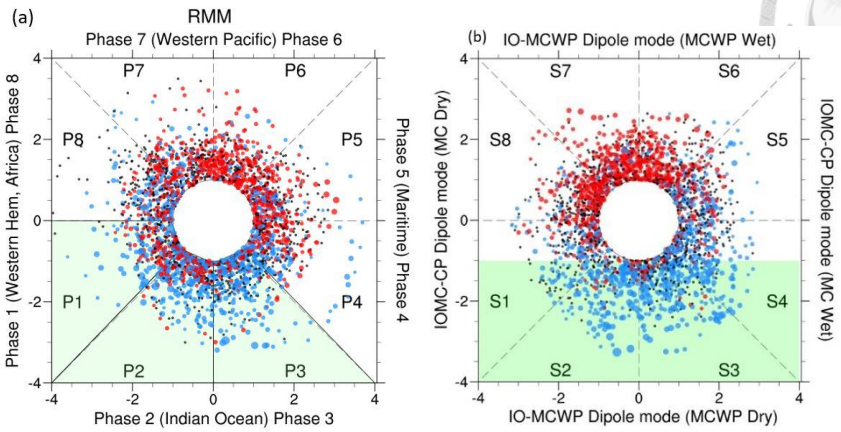

Figure 20 Rainfall anomalies in the EA region (110°E~150°E; 20°N~35°N) displayed in the (PC1, PC2) phase space based on (a) RMM, and (b) SVD indices.

doi:10.6342/NTU202303152

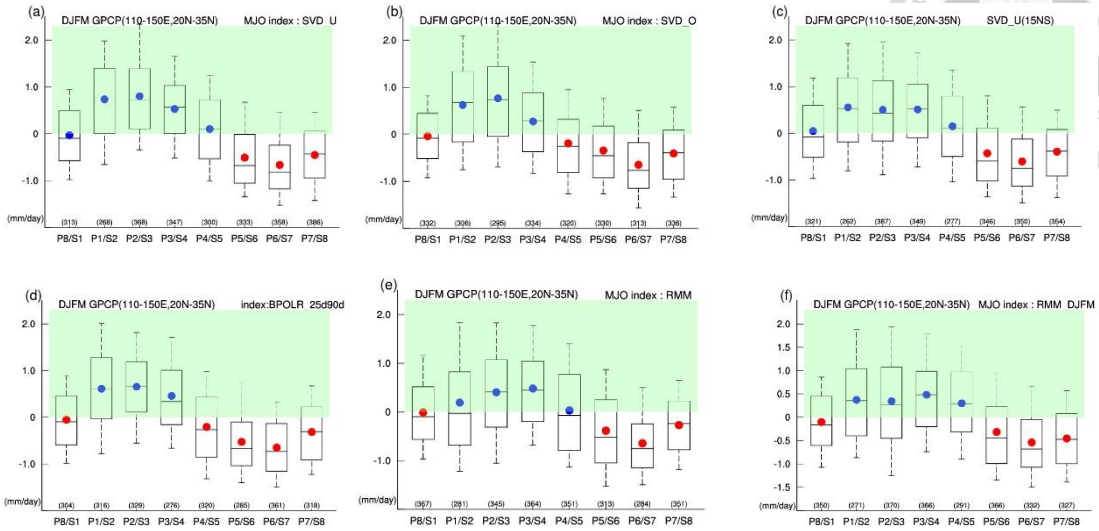

Figure 21　Probability distribution of rainfall anomalies within the EA region in the 8 phases of MJO defined by different approaches: (a) SVD_U index (b) SVD_O index (c) SVD_U index based on data within 15ºS–15ºN (d) BPOLR_25–90d index (e) All-season RMM index (f) RMM DJFM index.

doi:10.6342/NTU202303152

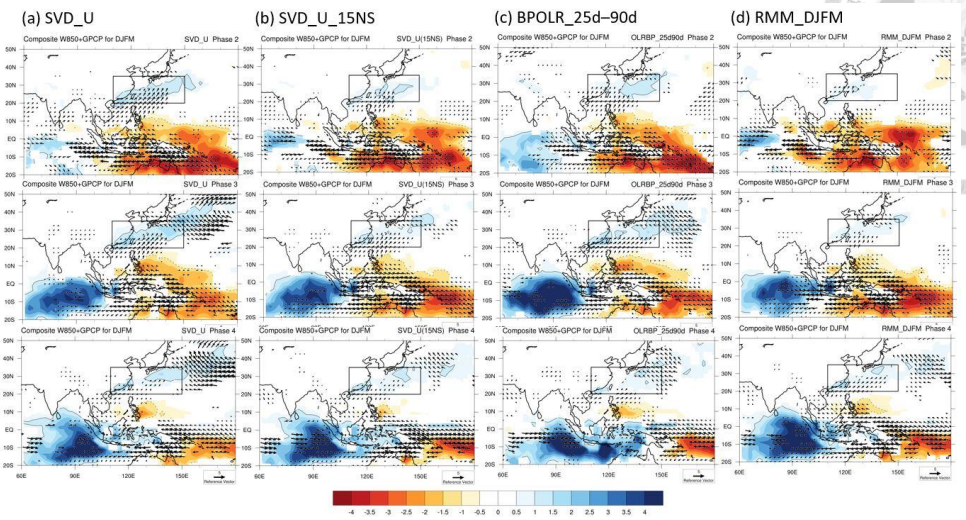

Figure 22　MJO phase composite fields of anomalous GPCP rainfall and winds at 850-hPa for phase S2–S4 (WH04 RMM phase P1–P3, from top to bottom): (a) SVD_U, (b) SVD_U index based on data within 15ºS–15ºN, (c) 25–90-day filtered OLR, (d) RMM_DJFM.

doi:10.6342/NTU202303152

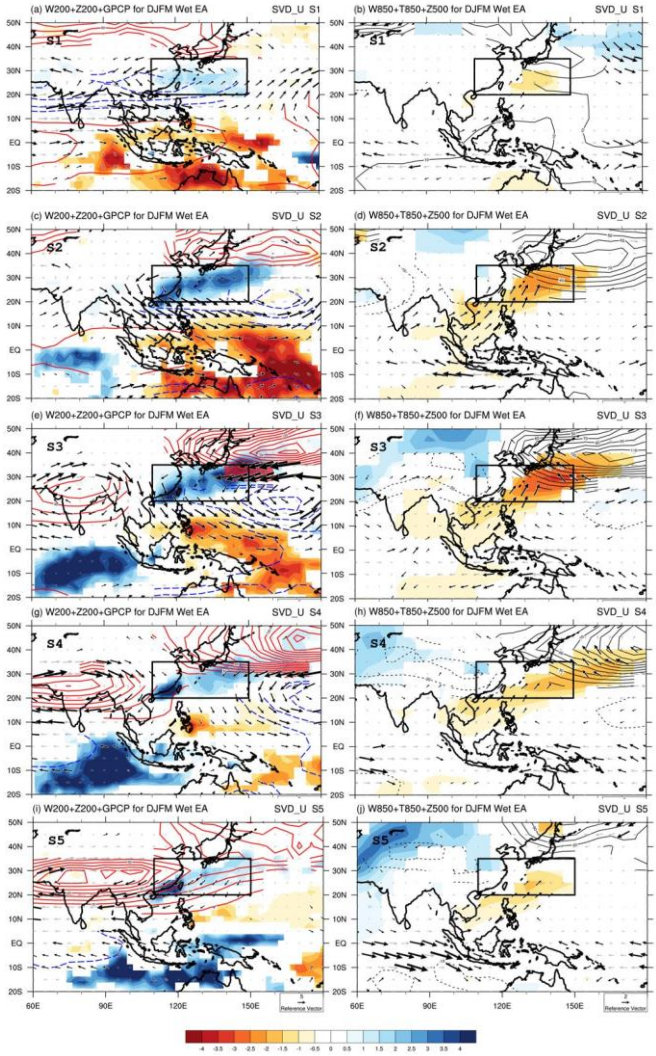

Figure 23 Anomalous fields of GPCP rainfall (shaded), 200-hPa height (contour) and 200-hPa wind (arrow) composite for SVD phase (a) S1, (c) S2, (e) S3, (g) S4, (i) S5, for days the EA rainfall larger than the threshold at top 1/3 of frequency distribution of daily GPCP rainfall averaged in East Asia (20°N–35°N,110°E–150°E). (b, d, f, h, j) the same as (a, c, e, g, i) except for 850-hPa temperatures (shaded), 500-hPa height (contour) and 850-hPa wind (black arrow).

doi:10.6342/NTU202303152

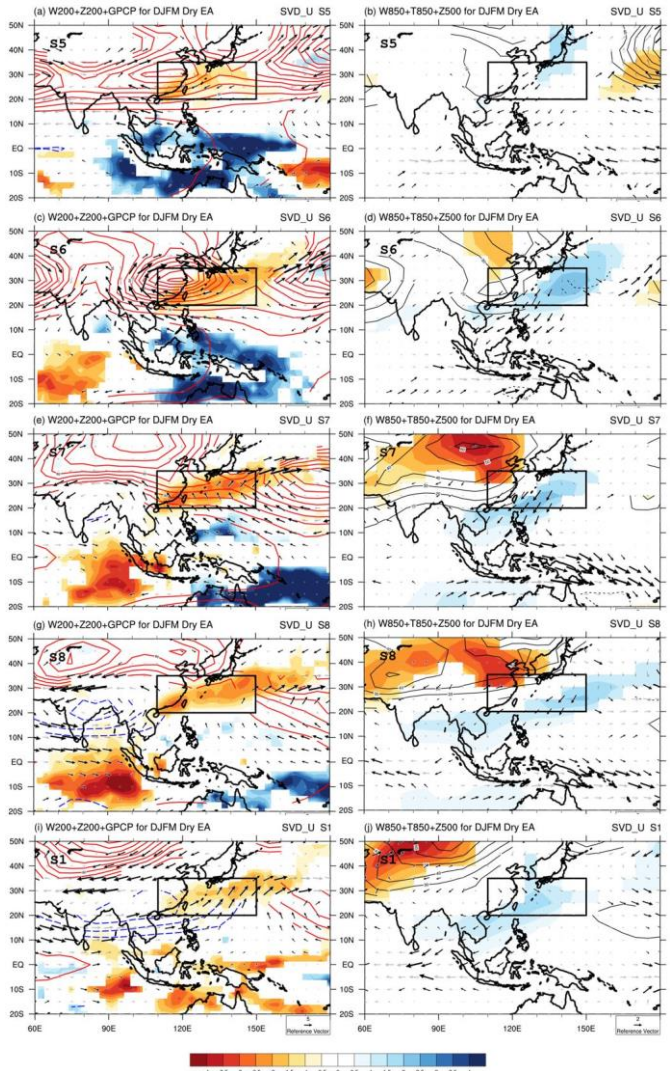

Figure 24　Same as Fig. 23, except for SVD phase S5, S6, S7, S8, S1 for days the EA rainfall smaller than the threshold at bottom 1/3 of frequency distribution of daily GPCP rainfall averaged in East Asia (20ºN–35ºN,110ºE–150ºE).

doi:10.6342/NTU202303152

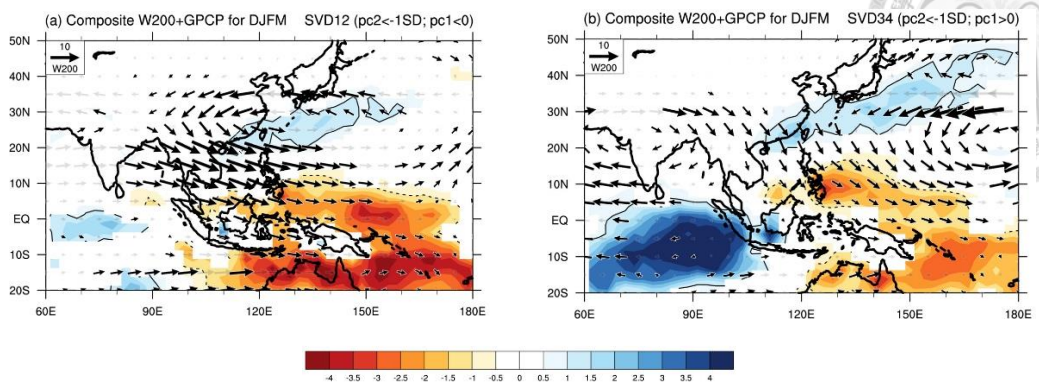

Figure 25 Composite fields of anomalous GPCP rainfall and 200-hPa winds for the days when PC2 of the SVD analysis < 1σ and (a) PC1 < 0, (b) PC1 > 0.

doi:10.6342/NTU202303152

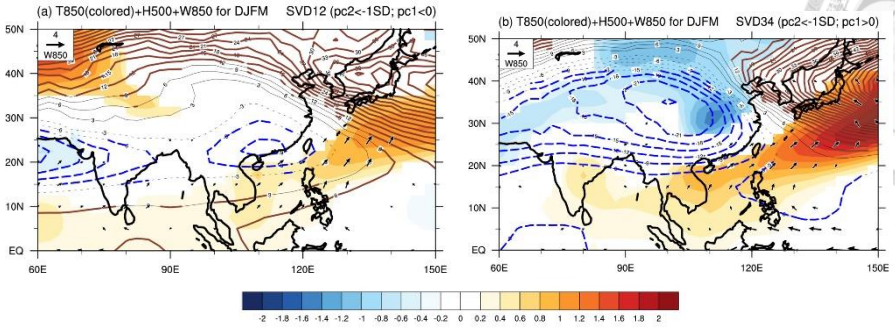

Figure 26 Same as Fig. 25, except for anomalous temperature at 850-hPa (colored) and heights at 500-hPa (contoured) and 850-hPa winds (vector).

doi:10.6342/NTU202303152

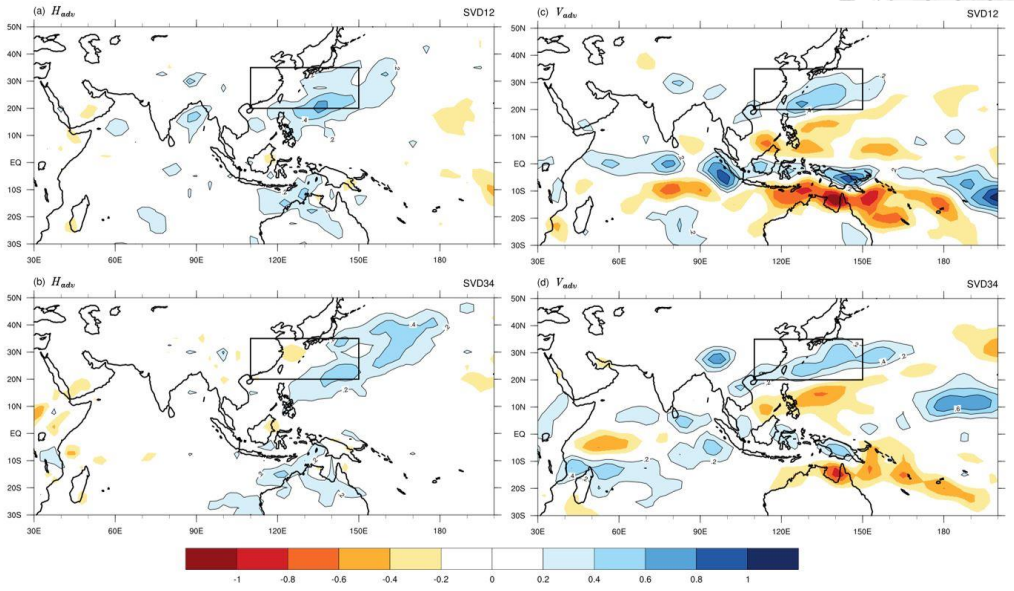

Figure 27 The horizontal fields of vertically integrated moisture budget: (a),(b) horizontal advection for SVD12 and SVD34 and (c),(d) vertical advection for SVD12 and SVD34 (units are g $kg^{-1}day^{-1}$). The positive values are shaded and also contoured.

doi:10.6342/NTU202303152

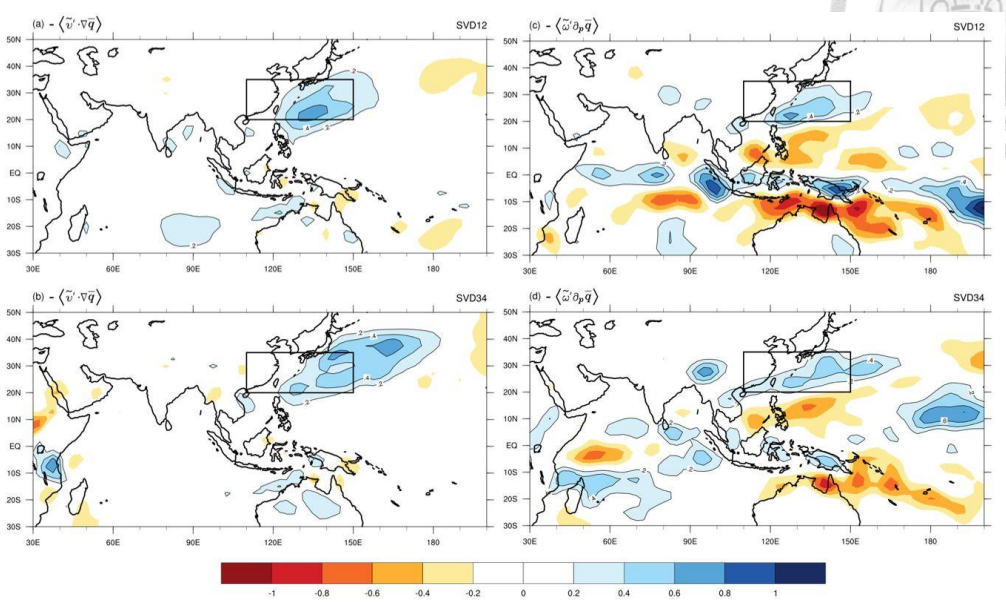

Figure 28 As in Fig. 27, but for the dominant component $-(<\widetilde{\boldsymbol{v}'}\cdot\nabla\bar{q}>)$ and $-(<\widetilde{\omega'}\partial_p\bar{q}>)$(g kg^{-1}day^{-1}). The positive values are shaded and also contoured.

doi:10.6342/NTU202303152

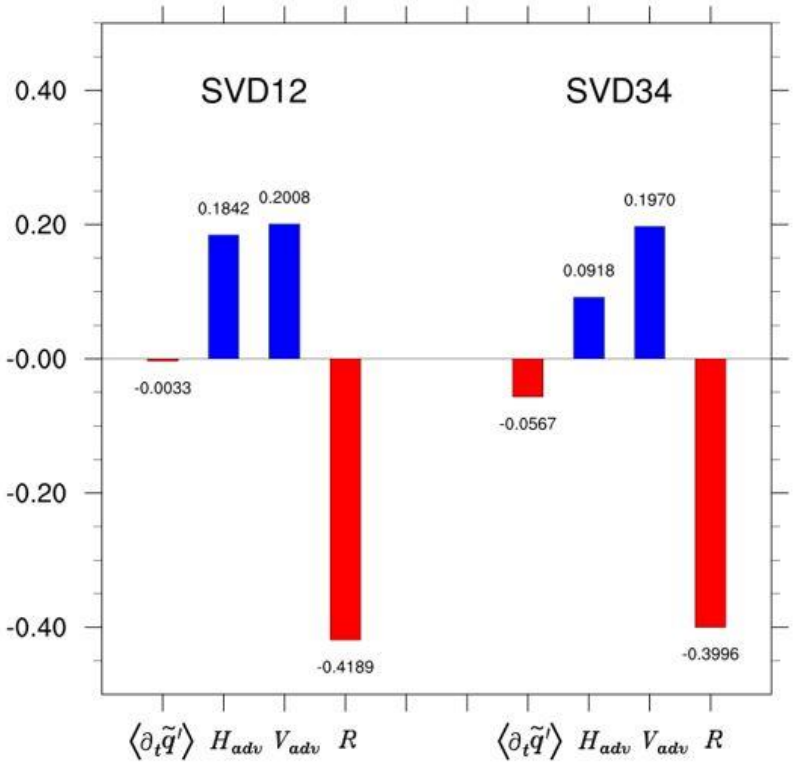

Figure 29 The areal mean of vertically integrated moisture budget within the EA region (110ºE–150ºE, 20ºN–35ºN) for SVD phase 1–2 and SVD phase 3–4. The budget terms shown include the tendency, Hadv, Vadv, and $R = -L^{-1}(< \widetilde{Q_2} > - \overline{Q_2})$ (units are g kg^{-1}day^{-1}).

doi:10.6342/NTU202303152

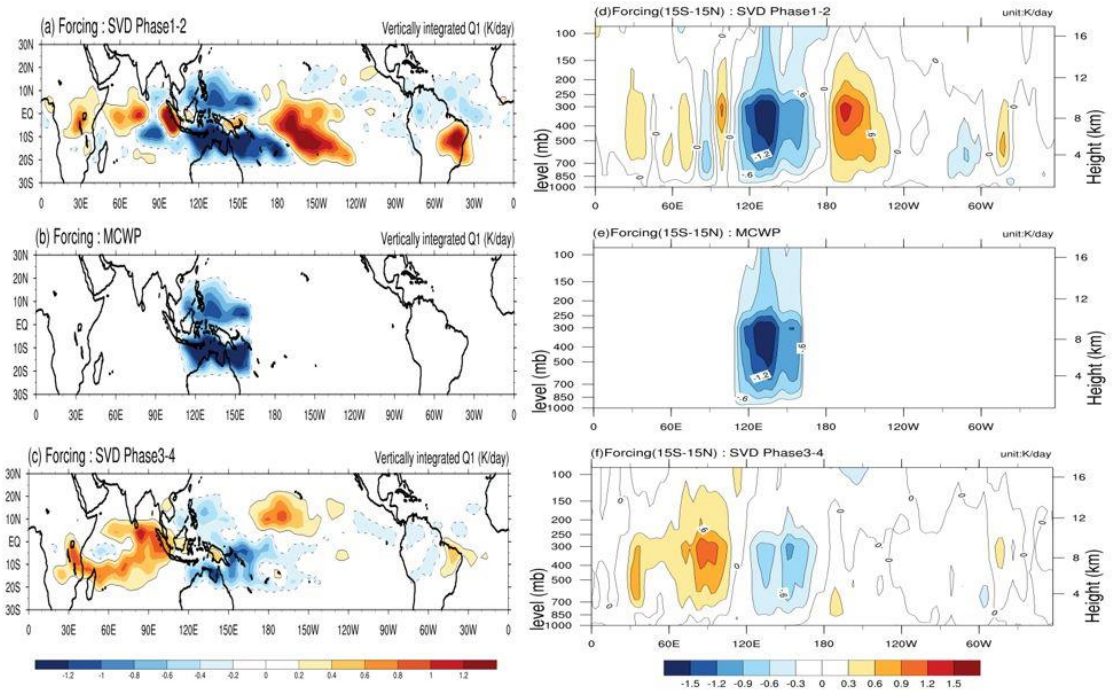

Figure 30 (a)–(c) The horizontal distribution of vertically integrated Q_1' and (d)–(f) the vertical–zonal distribution of latitudinally averaged Q_1' within 15°S–15°N for SVD12, MCWP, and SVD34, respectively. Units are K day^{-1}. Thin solid and dashed lines enclosing the heating and cooling fields in (a)–(c) are 0.2 and −0.2 K day^{-1} contours.

doi:10.6342/NTU202303152

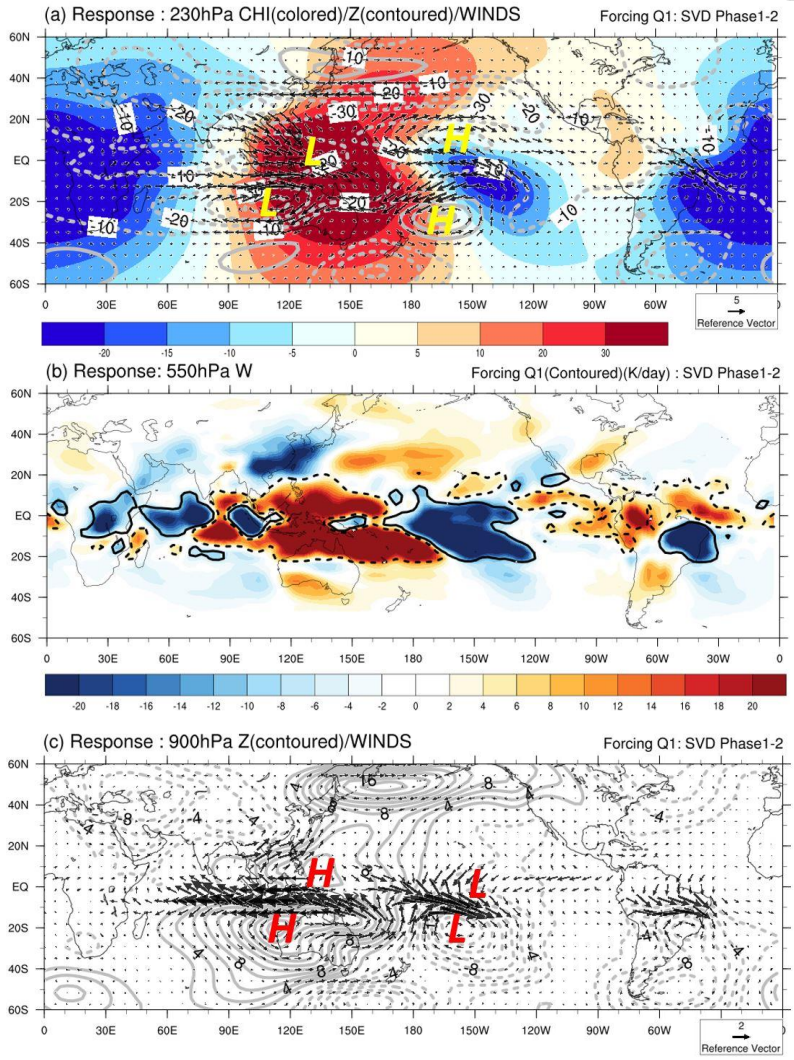

Figure 31. Model simulated fields in SVD12 (a) horizontal wind (vectors), height (contour; interval 10 m), and velocity potential (shading) at 230 hPa, (b) vertical velocity at 550 hPa (shading) along with $Q_1' = 0.2$ and -0.2 K day^{-1} contours (as in Fig. 30a), and (c) horizontal wind (vectors), height (contour; interval 2 m) at 900 hPa.

doi:10.6342/NTU202303152

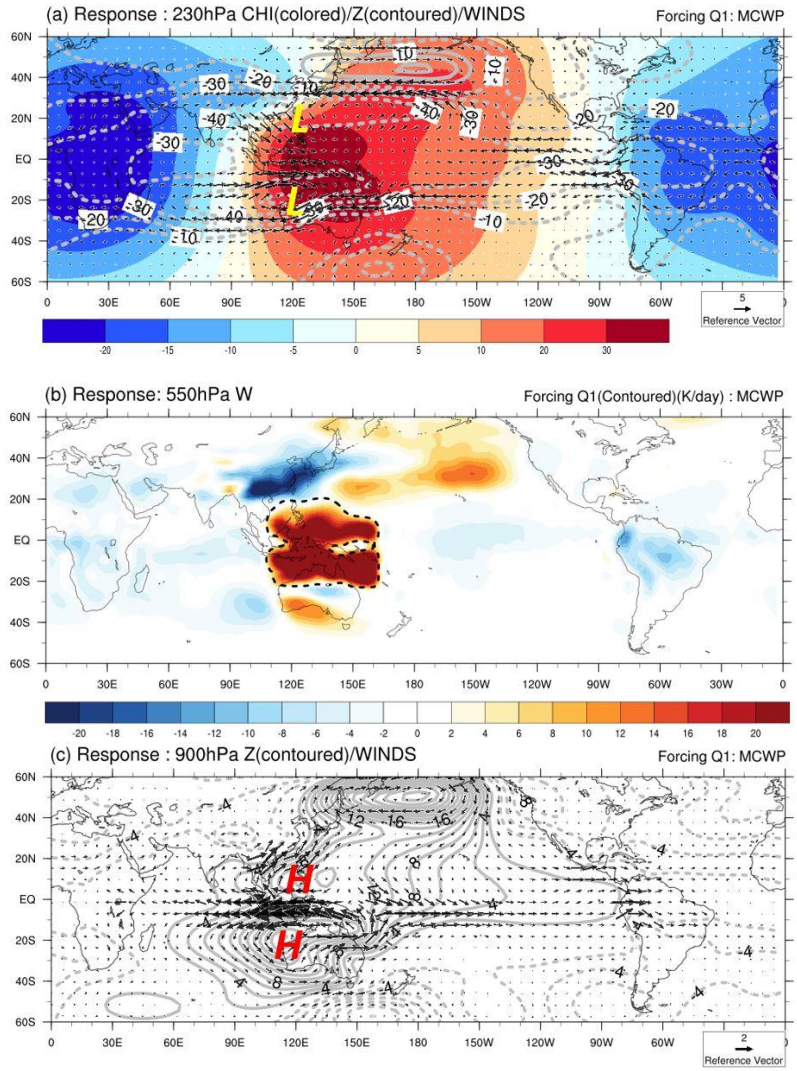

Figure 32 As in Fig. 31, but for MCWP.

doi:10.6342/NTU202303152

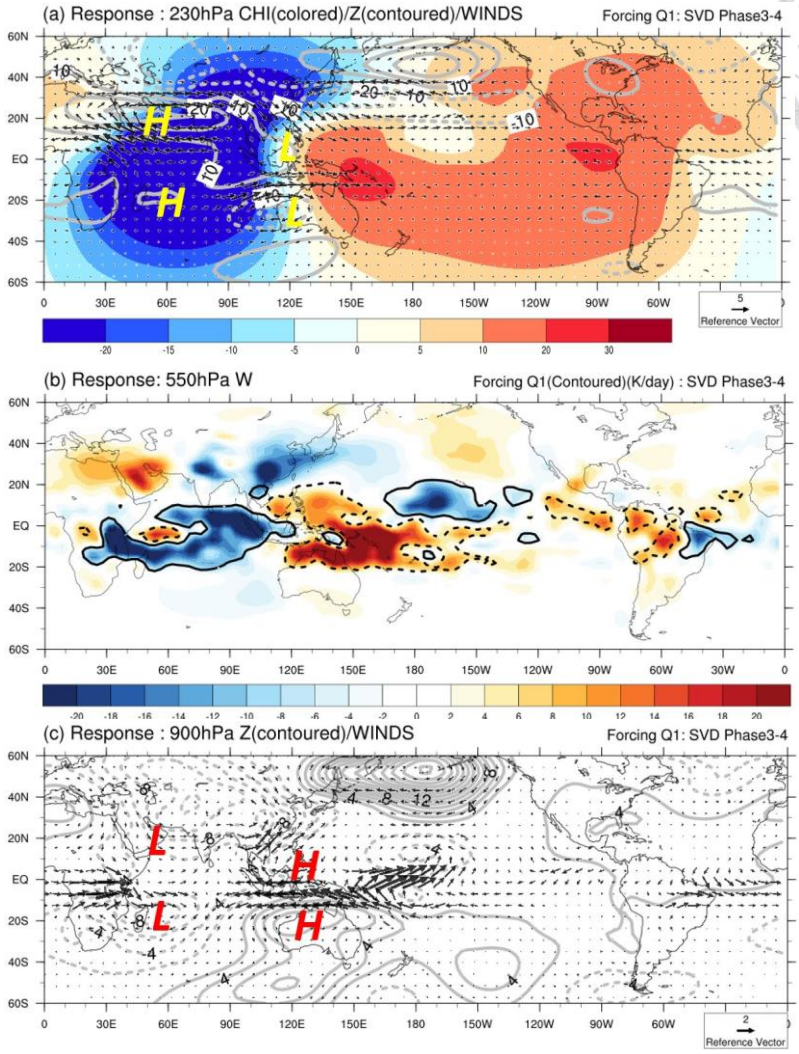

Figure 33 As in Fig. 31, but for SVD34.

doi:10.6342/NTU202303152

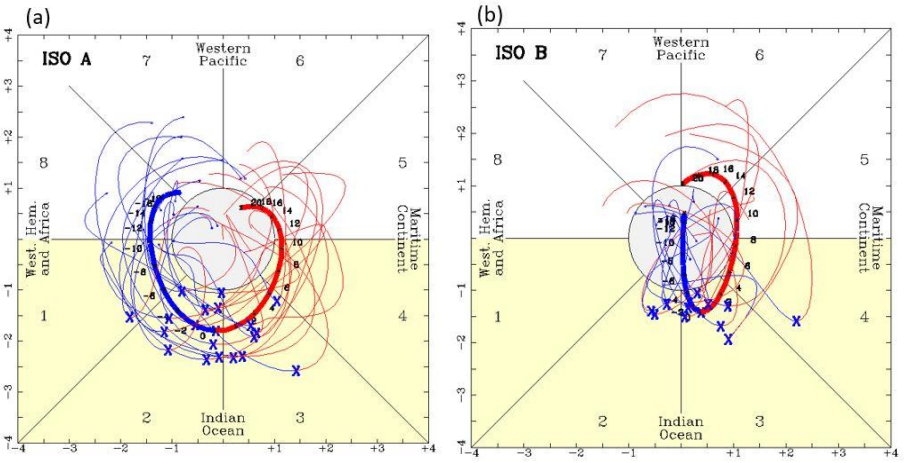

Figure 34 The MJO phase diagram for (a) 19 ISO-A and (b) 12 ISO-B events.

doi:10.6342/NTU202303152

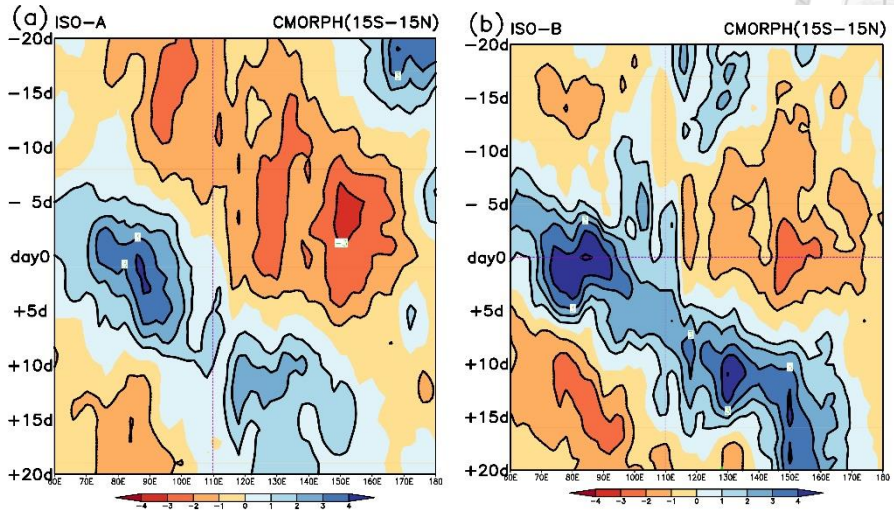

Figure 35 Composite evolution of averaged tropical (15°S-15°N) rainfall anomalies for (a) ISO-A and (b) ISO-B events.

doi:10.6342/NTU202303152

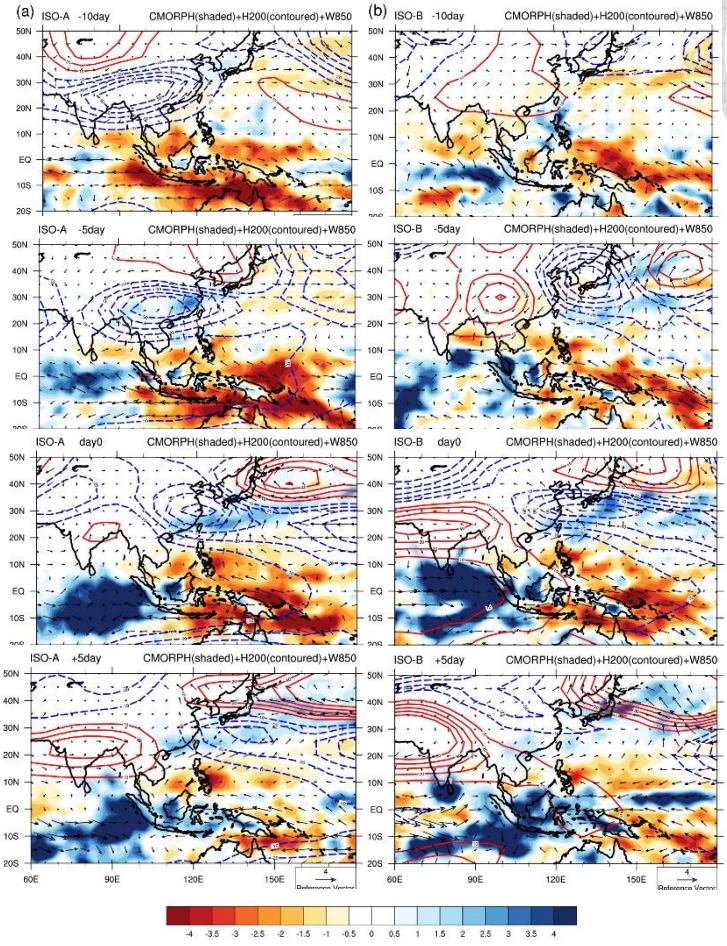

Figure 36 Composite evolution of rainfall, 200-hPa height, and 850-hPa winds at day -10, -5, 0, +5 for (a) ISO-A and (b) ISO-B events.

doi:10.6342/NTU202303152

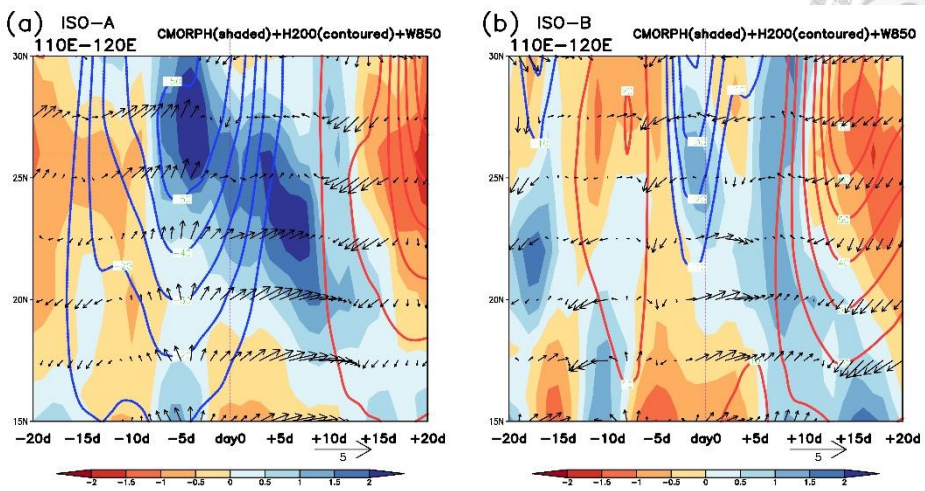

Figure 37　Composite time-longitude section of rainfall, 200-hPa height, and 850-hPa winds averaged within 110ºE-120ºE for (a) ISO-A and (b) ISO-B events.

doi:10.6342/NTU202303152

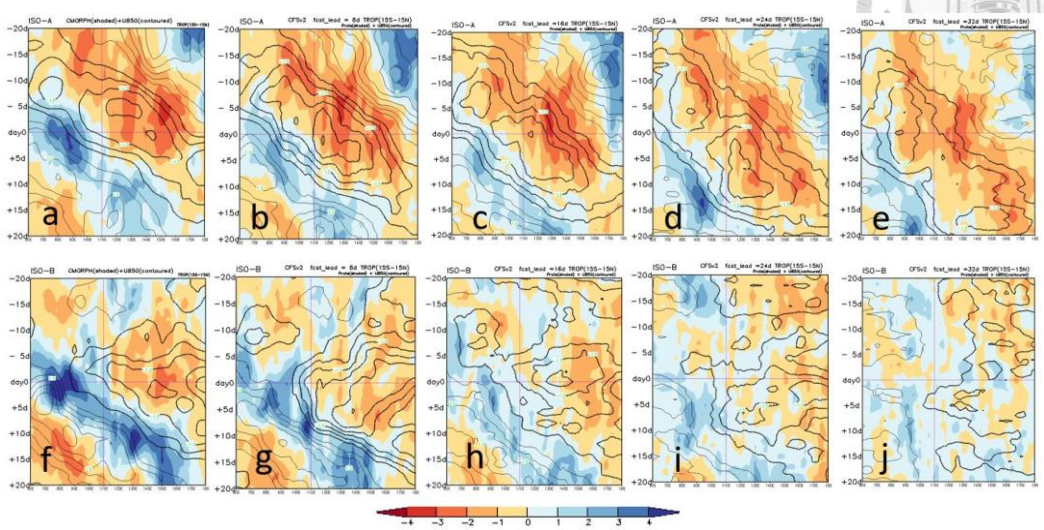

Figure 38　Composite evolution of averaged tropical (15°S–15°N) rainfall and 850-hPa zonal wind anomalies in time (day -20 to day 20) and longitude (80°E-180) for (a) observations and NCEP CFSv2 forecasts at lead time (b) 8 days (c) 16 days, (d) 24 days (e) 32 days for ISO-A events. (f)-(j) same as (a)-(e) except for ISO-B events.

doi:10.6342/NTU202303152

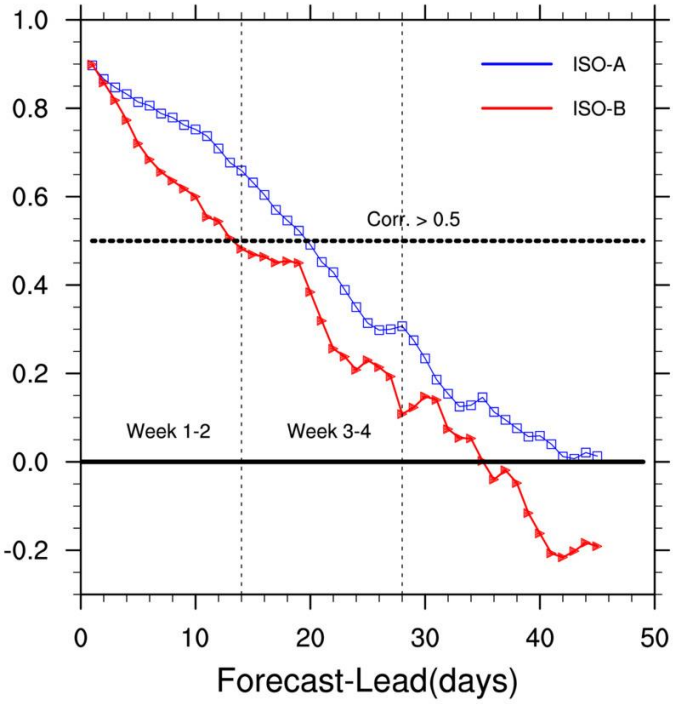

Figure 39 The pattern correlation between the observation and NCEP CFSv2 forecast of rainfall evolution in time (day -20 to day 20) and longitude (80ºE-180) as in Fig. 38. The forecast lead time ranges from day 0 to day 45. The pattern correlations for ISO-A and ISO-B are shown in blue and red, respectively.

doi:10.6342/NTU202303152

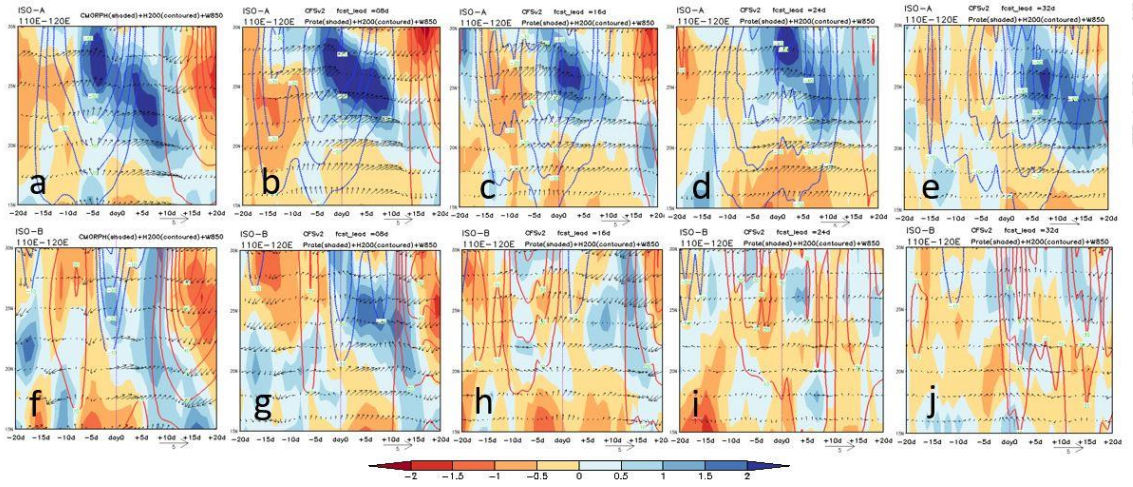

Figure 40　The time-latitude section over 15ºN–30ºN of rainfall anomalies (colored) and 200-hPa height anomalies (contour) and 850-hPa winds (vector) averaged over 110ºE–120ºE for (a) observations and NCEP CFSv2 forecasts at lead time (b) 8 days (c) 16 days, (d) 24 days (e) 32 days for ISO-A events. (f)-(j) same as (a)-(e) except for ISO-B events.

doi:10.6342/NTU202303152